Materials & Design 266 (2026) 116014

Contents lists available at ScienceDirect

Materials & Design

journal homepage: www.elsevier.com/locate/matdes

Investigation of IG copper precipitation behaviour and its impact on GBs in ferritic steels

Asmaa Elbeltagy [a,*], Alexander Gramlich [a,*], Milan Heczko [b], Antonín Dlouhý [b], Tomáš Kruml [b], Piotr Warczok [c], Ernst Kozeschnik [d], Ulrich Krupp [a]

[a] Steel Institute (IEHK), RWTH Aachen University, Germany
[b] Institute of Physics of Materials, Czech Academy of Sciences, Žižkova 22, 61600 Brno, Czech Republic
[c] MatCalc Engineering GmbH, Gumpendorferstraße 21, 1060 Wien, Austria
[d] Institute of Materials Science and Technology, Wien, TU, Austria

ARTICLE INFO

Keywords:
Cu precipitation
IG precipitation
Precipitates free zone
Sustainability
Ferritic steels

ABSTRACT

This study presents a comprehensive investigation of copper precipitation at ferrite–ferrite grain boundaries (GBs) containing intergranular (IG) cementite (Fe_3C) in a Cu-alloyed 0.2C ferritic steel (Fe–0.2C–2.0Ni–2.0Cu–0.5Mn, wt.%). The alloy was austenitized at 900 °C and aged at 550 °C for up to 2400 s. Correlative atom probe tomography (APT) and high-resolution scanning transmission electron microscopy (STEM) demonstrate that Cu precipitation at GBs differs fundamentally from that in the matrix. While matrix precipitates follow the classical martensitic Cu precipitation sequence, C-enriched GBs decorated with IG Fe_3C promote the formation of large disc-shaped FCC Cu precipitates (~50 × 15 nm). Their development generates Cu- and C-depleted zones (DZs) and precipitation-free zones (PFZs) adjacent to GBs, resulting in an estimated ~ 550 MPa loss in local strengthening near the GB, based on conventional models. By integrating experimental observations, modeled kinetics, IG Fe_3C characteristics, and GB chemistry, an evidence-based mechanistic interpretation is proposed to rationalize the coupled formation of IG Fe_3C and FCC Cu discs and their association with GB softening. These findings provide deeper insight into copper precipitation at GBs and its correlation with GB chemistry and local strengthening behavior.

1. Introduction

Copper as a steel alloying element has been widely investigated in the last century due to its ability to enhance the mechanical [1], corrosion [2,3], and antibacterial properties [4,5] in steels. Recently, with growing interest in the circular economy, and due to the increasing concentration of Cu in recycled steels, this attention has grown again, as the production of future high-strength sheet steels is significantly dependent on the control of impurities [6,7], as they might cause critical embrittlement during the processing. Caused by the low solubility of copper in the ferrite compared to austenite [8–11], Cu tends to form copper-rich precipitates solely or alongside other alloying elements in the ferritic matrix [12–15]. Due to its tunability, copper precipitates (Cu-PPts) have the ability to enhance both static and dynamic mechanical properties [16–18]. Various research works focused on copper-alloyed steels have shown enhanced yield strength and ultimate tensile strength through precipitation hardening [6,19–21] and enhanced toughness and work hardening ability [22,23] attributed to the interaction nature between the Cu-PPts and the surrounding dislocations [24–26]. The positive impact of Cu-PPt on fatigue properties, such as defect tolerance and fatigue life, was investigated and linked to the ability of Cu-PPts to extend the work hardening with heavily jogged dislocation arrangements. Softening is eliminated [27] by (i) replacing the formation of cell dislocations by vein-like and planar dislocations structures [28–30], (ii) the tendency of the Cu-PPts to produce a more homogenous plastic zone, and (iii) the ability to diffuse the strain localization [31,32]. Interchangeably, increasing the size and the number density of Cu-PPts extends the fatigue life significantly by inducing a higher work hardening exponent ($|e_{II}|$) and increasing the deformation exponent (R^2) [33–35].

The tunability of copper precipitation, which enables the enhancement and control of the desired mechanical properties of the alloy, evolves from the unique copper precipitation and evolution mechanism that depends on the surrounding matrix, the copper concentration, and

* Corresponding authors.
E-mail addresses: asmaa.elbeltagy@iehk.rwth-aachen.de (A. Elbeltagy), alexander.gramlich@iehk.rwth-aachen.de (A. Gramlich).

https://doi.org/10.1016/j.matdes.2026.116014
Received 30 January 2026; Received in revised form 8 April 2026; Accepted 13 April 2026
Available online 15 April 2026

the aging time. Thus, the understanding of this precipitation mechanism is of fundamental importance from the perspective of alloy design focused on the achievement of desired mechanical properties. In austenitic steels, the copper precipitation mechanism is induced by the large positive enthalpy of mixing in the Fe-Cu system [36] and driven by copper diffusion from the matrix into the copper precipitates. Studies on this phenomenon have shown that the copper precipitation mechanism in austenite consists of three stages: (i) nucleation, (ii) growth, and (iii) coarsening. The first is the nucleation of the compositionally nearly 100 at.% Cu-enriched precipitates with face-centered cubic (FCC) crystal lattice, later followed by the coarsening of these precipitates [37]. The coarsening process according to the Ostwald ripening [38] is usually simulated using the Umantsev and Olsen [39] model, which is based on the Lifshitz-Slyozov-Wagner (LSW) theory.

Unlike the simple copper precipitation mechanism occurring in the austenitic matrix, the copper precipitation mechanism in ferrite is more complex. In ferrite, copper precipitation takes place through a series of displacive (martensitic) transformations (BCC → 3R → 9R → FCC) [40,41]. At the beginning of the aging process and due to the low solubility of the copper in the surrounding ferrite matrix, coherent metastable nano-ordered body-centered cubic (BCC) Fe–Cu precipitates of a diameter up to approximately 5 nm [41] are formed, manifesting themselves through super lattice reflections in diffraction patterns during the high-resolution transmission electron microscopy (HRTEM) investigation [42]. With increasing copper diffusion into the core, Cu-PPts grow in size, become more disordered, and eventually, lose their coherency [42]. Due to the increased disorder and the lattice misfit between the Cu-PPts and the surrounding ferritic matrix [41], the BCC Cu-PPts transform into twinned or untwined 9R crystal structure, which are known by the "herring-bone" fringes upon transmission electron microscopy (TEM) investigation and the stacking fault detected by the HRTEM, reflecting a close-packed structure with a stacking sequence of ABC–BCA–CAB–A through a displacive transformation [40]. The formation of twins and other stacking faults in the 9R Cu-PPts is found to be driven by the need to reduce the coherency strain energy of the 9R precipitates and the adaptation of the lattice transformation from BCC to 9R [40,41,43]. With extended aging time and precipitation growth, the 9R Cu-PPts could transform to 3R Cu-PPts [41] through a Shockley-type partial dislocation, to the twinned FCC precipitates [40], or directly to the stable Cu–FCC precipitates through a structure relaxation mechanism where stacking faults are eliminated.

Furthermore, the effect of other alloying elements, such as Ni, Al, and Mn, on the copper precipitation mechanism has also been widely studied and found to have an impact on the precipitation kinetics, nucleation, and coarsening behaviour. When comparing the purely copper-alloyed steels to those with Ni, Al, and Mn additions, it is found that the copper precipitation nucleation energy decreases, leading to an increased nucleation rate [44,45]. The higher additions of Ni, Al, and Mn hinder the coarsening of the Cu-PPts and lower the coarsening coefficient according to the LSW theory [44]. The reduced coarsening rate of the Cu-PPts is caused by the segregation of Ni, Al, and Mn to the Cu-PPts/matrix interface [12,19,20,45] and the formation of NiAl or NiMn–B2 shells that act as a barrier against copper diffusion into the Cu-PPts [44]. Additionally, the copper precipitation kinetics have been evaluated through the application of Monte Carlo simulations [46,47] according to the LSW theory [48,49], small-angle neutron scattering (SANS) [50], differential scanning calorimetry (DSC) [51,52], electrical resistivity [53,54], and hardness [55].

Although the mechanisms of copper precipitation have been extensively investigated with respect to aging time, temperature, and the influence of alloying elements, very limited attention has been given to copper precipitation occurring at ferrite–ferrite grain boundaries (GBs), particularly in the presence of intergranular (IG) cementite (Fe_3C) and/or carbon enrichment. In particular, the precipitation characteristics, evolution mechanisms, and their impact on the GB strength remain insufficiently understood.

Therefore, this research work, for the first time, sheds light on the copper precipitation phenomena occurring at ferrite-ferrite GB in the presence of IG Fe_3C, revealing their effects on GB chemical composition and the consequent changes in boundary strength, based on a correlative analysis using high-resolution scanning transmission electron microscopy (STEM), atom probe tomography (APT), and MatCalc precipitation-kinetics modeling. The results are further correlated and discussed with the goal of explaining the crack initiation behaviour previously reported for the same alloy system [35]. This work provides a novel, multi-scale understanding of copper precipitation at ferrite-ferrite GBs in the presence of IG Fe_3C. It uniquely demonstrates how copper behaves at GBs under complex local chemistries and establishes a direct mechanistic framework that describes both its precipitation behavior and the link between these nanoscale processes and GB weakening, leading to crack initiation.

2. Experimental details

2.1. Materials and processing

The nominal chemical composition of X21 steel alloy investigated in this study is listed in Table 1 in weight percentage (wt.%) and atomic percentage (at.%). The ingot was homogenized at 1250 °C for 2 h before open-die forging. The blocks were subsequently forged in the Semi-Product Simulation Centre (SPSC) at IEHK using a 400-ton hydraulic press (Weidemann) at a ram speed of 40 mm s^{-1} to produce two billets with final dimensions of 60 mm × 60 mm × 1000 mm, using a reduction percent per pass of approximately 26 − 27%. In the first forging stage, the initial cross-section was reduced from 140 mm × 140 mm × 500 mm to 90 mm × 90 mm × 1200 mm. This reduction was achieved by applying two forging rounds to one end of the billet, with each round consisting of two passes and a 90° rotation of the ingot between passes. The ingot was then reheated to 1250 °C, and the same procedure was applied to the opposite end. After reaching a size of 90 mm × 90 mm × 1200 mm, the bar was divided into two pieces and reheated to 1250 °C. The same forging routine was repeated to further reduce the cross-section from 90 mm × 90 mm to 60 mm × 60 mm. In this stage, two forging rounds were applied to one end of the half-bar, followed by reheating and repeating the procedure on the opposite end.

During forging, the surface temperature was monitored with a pyrometer, indicating an average drop of approximately 160 °C per forging round. The forging schedule reported in Table S1 corresponds to one end of the billet, while the same sequence was subsequently applied to the opposite end. Further details of the thermal history are provided in Table S1 in the supplementary material. After forging, the billets were air-cooled to room temperature for approximately 36 h. In the forging schedule, the temperature drop per pass is defined as the difference between the temperature measured immediately before and after each pass, whereas the cooling per round corresponds to the difference between the temperature at the beginning of the first pass and the temperature at the end of the second pass, just before reheating. To improve readability and account for measurement scatter, all recorded temperatures were rounded to the nearest 5 °C: values ending in 1–2 °C were rounded down to 0 °C, and values ending in 3–4 °C were rounded up to 5 °C. To produce the different conditions and states of Cu-PPts and matrix microstructure, the samples were austenitized at 900 °C for 13 min, then subjected to an isothermal holding temperature of 550 °C for 120 s and 2400 s, respectively (shown in Fig. 2a).

Selected samples designated with a combination of steel grade and

Table 1
Chemical composition of the investigated steel (in wt.% and at.%).

	C	Mn	Si	Cr	Cu	Al	Ni	Fe
wt.%	0.21	0.52	0.01	0.02	2.01	0.04	2.00	Bal.
at.%	0.97	0.53	0.02	0.02	1.76	0.08	1.89	Bal.

aging time, specifically 120 s and 2400 s conditions, were subjected to the multidisciplinary and multi-scale microstructural characterisation using the scanning electron microscope (SEM).

2.2. Microstructural characterisation

The microstructure of the aged X21 steel was examined using light optical microscopy (LOM, Leitz Aristomet) and SEM equipped with an electron backscatter-diffraction (EBSD) detector (Oxford Instruments). The specimens were ground using SiC abrasive papers up to 4000 grit, followed by mechanical polishing with 3 μm and 1 μm diamond suspensions. Final surface finishing was performed using an OPS (oxide polishing suspension) colloidal silica. EBSD measurements were conducted at an accelerating voltage of 20 kV, a step size of 50 nm, and a working distance of approximately 18 mm. Postprocessing and indexing were carried out using Aztec software (version 3.3, Oxford Instruments).

2.2.1. Atom probe tomography (APT) measurements

Three-dimensional (3D) characterisation of Cu-PPts and the surrounding matrix chemistry was carried out using APT (LEAP 4000X HR, CAMECA Instruments Inc.). Data were collected in laser-pulsing mode (wavelength 355 nm, repetition rate 200 kHz, pulse energy 30 pJ). The APT specimens (tips) were prepared by site-specific lift-out using the Easy-Lift method followed by annular milling in a dual-beam focused-ion-beam/scanning electron microscope (FIB/SEM, FEI Helios Nanolab 660). Data reconstruction and analysis were performed using the AP Suite software.

2.2.2. High-resolution scanning transmission electron microscopy (HR-STEM)

A combination of SEM backscattered electron (BSE) imaging, EBSD, and FIB was used to identify the sites of interest in the microstructure. Field emission gun (FEG) operated TESCAN Lyra 3 XMU SEM equipped with FIB was used to extract site- and orientation-specific TEM thin foils (lamellae) with normal vector of the foil plane parallel to ⟨001⟩ crystallographic directions of the ferrite matrix. These foils were subsequently investigated using Thermo Fisher Scientific (TFS) Talos F200i STEM operating at 200 kV and also image-aberration corrected and monochromated TFS Titan-Themis STEM operating at 300 kV. The TEM thin foils were tilted into specific low-index crystallographic zones to perform atomic resolution imaging of the studied microstructures. Data were collected with TFS Titan-Themis using a high-angle annular dark-field (HAADF) detector and low camera length (73 mm) to emphasize Z-contrast of the phases. Defects and phases were also imaged by low-angle annular dark-field (LAADF) STEM or by two-beam diffraction contrast imaging (DCI) using both bright field (BF) and annular dark field (ADF) STEM detectors [56]. By simply adjusting the microscope camera length, and thus the acceptance angle of the annular detector, it was possible to transition from HAADF Z-contrast imaging mode, performed by exclusively collecting electrons that have been scattered to high angles to the small-angle scattered electrons sensitive to defect contrast [57]. Chemical composition was analyzed from data collected by a Super-X energy dispersive X-ray spectroscopy (EDS) detector in TFS Titan-Themis. The data were collected and processed using the TFS Velox software. In particular, the raw data in the original spectral maps were quantified using a standard Cliff-Lorimer (K-factor) fit (default k-factors available in Velox were used as well as the Brown-Powell empirical ionization cross-section model), including absorption correction and background subtraction. The atomic resolution STEM images were corrected for possible drift and scanning beam distortions using the drift corrected frame integration (DCFI) function of Velox.

2.3. Precipitation kinetic simulation (MatCalc)

Simulation of precipitate kinetics was performed with MatCalc software (ver. 6.05.0125) [58,59]. The simulated temperature starts at 900 °C and decreases from the austenite region down to 550 °C, followed by isothermal holding for 1 h. An instantaneous austenite-to-ferrite transformation begins at approximately 790 °C according to the phase equilibrium diagram shown in Fig. S1 of the supplementary material. Ferrite grain size was taken from the presented measurement. The model description contained the Fe_3C and Cu-PPts. The following populations of Cu-PPts were distinguished in the simulation depending on their nucleation site:

- BCC-structure clusters forming homogenously in the ferrite grains (Cu-PPt_{BCC})
- 9R-structure precipitates forming from Cu-PPt_{BCC} clusters in a size range of 2–3 nm (Cu-PPt_{9R})
- FCC-structure precipitates forming from Cu-PPt_{9R} precipitates in a size range of 6–10 nm (Cu-PPt_{FCC})
- FCC-structure precipitates forming on the Fe_3C precipitate surface (Cu-$PPt_{FCC\text{-}Cem}$)
- FCC-structure precipitates forming on the GBs (Cu-$PPt_{FCC\text{-}GB}$)

Fe_3C precipitates were assumed to nucleate at the ferrite GB edges (joining lines of at least three grains).

Precipitates were represented with the size distribution consisting of 25 size classes within the framework of the numerical Kampmann–Wagner model [60]. Evolution of the individual class sizes and chemical compositions was evaluated with the SFFK model [61,62]. The definition of shape factors (ratio of cylinder height to its diameter) allows the model application for the treatment of the non-spherical precipitates [63]. Nucleation rates of precipitates nucleating directly from the matrix (relevant for Cu-PPt_{BCC}, Cu-$PPt_{FCC\text{-}GB}$, Cu-$PPt_{FCC\text{-}Cem}$, and Fe_3C precipitates) were calculated with classical nucleation theory (CNT) [64]. Precipitate-matrix interface energies were evaluated with the generalized broken bond (GBB) model, including the spherical shape and diffuse interface corrections [65–67]. Furthermore, additional terms for the evaluation of the critical nucleation energy were used for the precipitates forming by heterogeneous nucleation (Cu-$PPt_{FCC\text{-}GB}$, Cu-$PPt_{FCC\text{-}Cem}$, and Fe_3C) [68].

Formation of Cu-PPt_{9R} and Cu-PPt_{FCC}, which are created through transformation from the precursor phase (Cu-PPt_{BCC} and Cu-PPt_{9R}, respectively), is treated in a different manner, by which some fraction of the transformation "substrate" (precursor) precipitate size distribution was transferred to the transformation "product" phase. The fraction of the transferred "substrate" phase was linearly increasing between some defined minimum (zero fraction) and maximum (unity fraction) of the precipitate size class [69]. Moreover, size-class evolution was also treated with the coalescence model, accounting for the mobility of the smaller clusters due to their attraction to vacancies [70].

Model parameters for the Cu-PPts in the ferrite grain (Cu-PPt_{BCC}, Cu-PPt_{9R}, Cu-PPt_{FCC}) were adapted from Stechauner et al [69]. While parameters for the IG Fe_3C and Cu-PPts (Cu-$PPt_{FCC\text{-}GB}$, Cu-$PPt_{FCC\text{-}Cem}$) found in this work are based on the experimental measurements and observations, other parameters for Fe_3C kinetics, as shown in Table 2, were adjusted and optimized according to Fig. 1 to reproduce its formation by austenite decomposition. Chemical potentials and solution enthalpies were evaluated based on the assessment given in MatCalc thermodynamic database ME-Fe (ver. 1.4). Diffusion coefficients were evaluated based on the assessment given in MatCalc mobility database mc_fe (ver. 2.016).

3. Results

3.1. Microstructure characterisation

To investigate the microstructure in terms of grain size and phase fraction, LOM and EBSD were employed. The heat-treatment procedure illustrated in Fig. 2a, comprising austenitisation for thirteen minutes followed by aging at 550 °C for 120 s and 2400 s, produced a

Table 2
Parameter set used in MatCalc kinetic simulation for intragranular (matrix) and IG precipitates.

Intragranular (matrix) precipitates parameters Parameter	Cu-PPt_{BCC}	Cu-PPt_{9R}	Cu-PPt_{FCC}
Critical temperature for diffuse interface energy correction [K]	2600	N/A	N/A
Coalescence factor	0.01	0.10	0.10
Coalescence exponent	−0.2	−0.2	−0.2
Solute diffusion enhancement factor	15	4	1
IG precipitates parameters			
Parameter	**Cu-$PPt_{FCC-Cem}$**	**Cu-PPt_{FCC-GB}**	**Fe_3C**
Shape factor	0.333	0.333	0.003
Accounting for heterogeneous nucleation site energy	Yes ($\kappa_i = 0.75$)	Yes ($\kappa_i = 1.00$)	Yes ($\kappa_i = 1.00$)
Nucleation site efficiency factor	100	N/A	N/A
Solute diffusion enhancement factor	30	2	N/A

ferritic–pearlitic microstructure containing approximately 95% ferrite and 5% pearlite, as determined from the LOM observations shown in Fig. 2b and e.

The EBSD phase maps confirm a predominantly ferritic microstructure with 0.4% and 0.37% Fe_3C located along ferrite–ferrite GBs in the 120 s and 2400 s conditions, respectively, as can be seen in Fig. 2c and f. Grain size evolution was evaluated using the arithmetic mean of the maximum Feret diameter (MFD), as summarized in Table 3.

The EBSD results indicate that increasing the aging time exerts no significant influence on grain size, with arithmetic mean values of 4.5 μm and 4.7 μm for the 120 s and 2400 s conditions, respectively. The essentially unchanged grain size and ferrite–pearlite phase fraction confirm that prolonged aging has no noticeable effect on grain growth or overall microstructural evolution, consistent with expectations at this temperature range, where grain growth is not anticipated.

3.2. Atom probe tomography (APT)

APT was employed to analyse the matrix, ferrite–ferrite GBs, and pearlite–ferrite interface with respect to elemental partitioning, segregation, and precipitation behaviour, using elemental maps, proximity histograms for precipitation analysis, and one-dimensional concentration profiles for segregation and precipitation evaluation.

3.2.1. Elemental partitioning and matrix analysis

For a detailed analysis of grain and GB behaviour with respect to precipitation evolution and elemental partitioning, APT tips were extracted from the ferrite of the 120 s and 2400 s conditions, as indicated by the Pt depositions in the SEM images shown in Fig. 3.

In particular, APT analyses of three tips taken from the ferritic matrix of the 120 s condition, the ferrite–ferrite GB, and the ferrite–pearlite interface of the 2400 s condition are presented and discussed in this work. The resulting atomic distributions reveal the partitioning of Fe, C, Cu, Ni, and Mn within ferrite and pearlite, as well as across the ferrite–ferrite GBs and ferrite-pearlite interphase interfaces.

While the pearlite in Fig. 4 is characterised by a high carbon content and a lower iron content due to the presence of Fe_3C lamellae, the ferrite exhibits a markedly lower carbon concentration owing to the limited carbon solubility in the ferritic matrix. The ferrite matrices of the 120 s and 2400 s conditions, shown in Fig. 4.a and c, reveal the presence of Cu-PPts without any distinct segregation of manganese or nickel, which are typically known to form core–shell or co-precipitation behaviour with copper. In contrast, the pearlitic regions exhibit copper depletion accompanied by manganese segregation towards the ferrite–pearlite GB, which may be associated with the presence of a prior-austenite GB (PAGB).

A region of interest (ROI) cylinder was constructed within the ferritic matrix, in an area free of precipitates to exclude their influence on the matrix composition, and within the pearlitic matrix to determine elemental partitioning. As shown in Fig. 5a, the copper content in the ferritic matrix decreases with increasing aging time from 120 s to 2400 s. Specifically, the copper concentration in ferrite decreases from approximately 1.2 at.% to 0.4 at.%. Furthermore, while the ferritic matrix at 2400 s contains about 0.4 at.% Cu, the copper content in the pearlitic microstructure is substantially lower, at roughly 0.1 at.%. Nickel likewise decreases from 1.0 at.% in the ferritic matrix to 0.8 at.% in the pearlitic matrix at the same aging time of 2400 s Fig. 6.

The reduction in nickel and copper contents in pearlite compared with ferrite is attributed to their limited solubility in the C-enriched

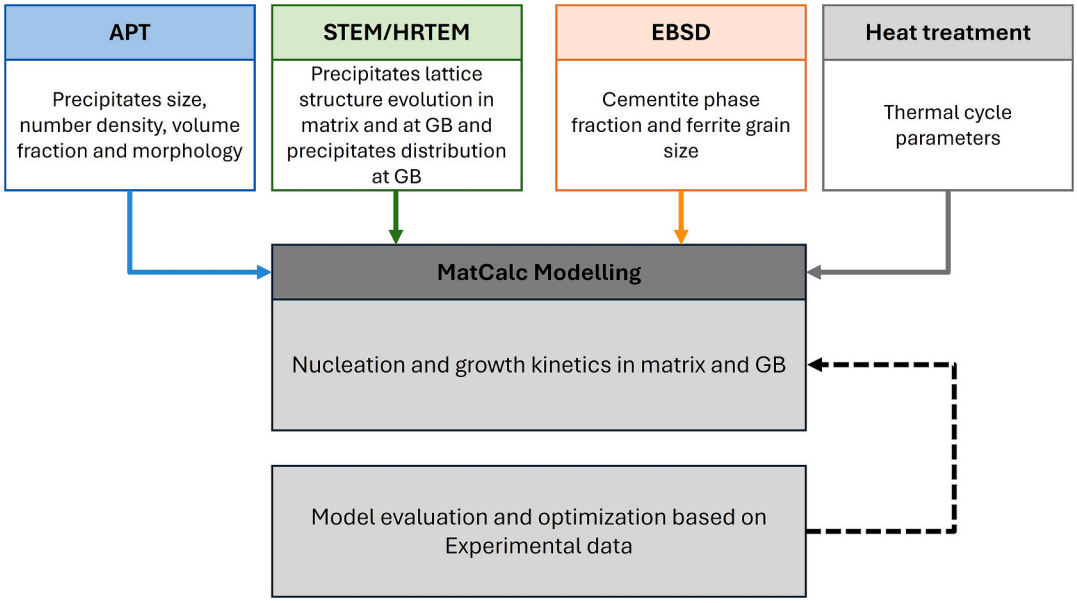

Fig. 1. Schematic workflow for integrated experimental and computational analysis of precipitation in ferritic steels, showing input of key APT, STEM/HRTEM, EBSD, and heat treatment data into MatCalc modelling to predict nucleation and growth kinetics of matrix and GB precipitates, followed by model evaluation and optimisation based on comparison with experimental measurements.

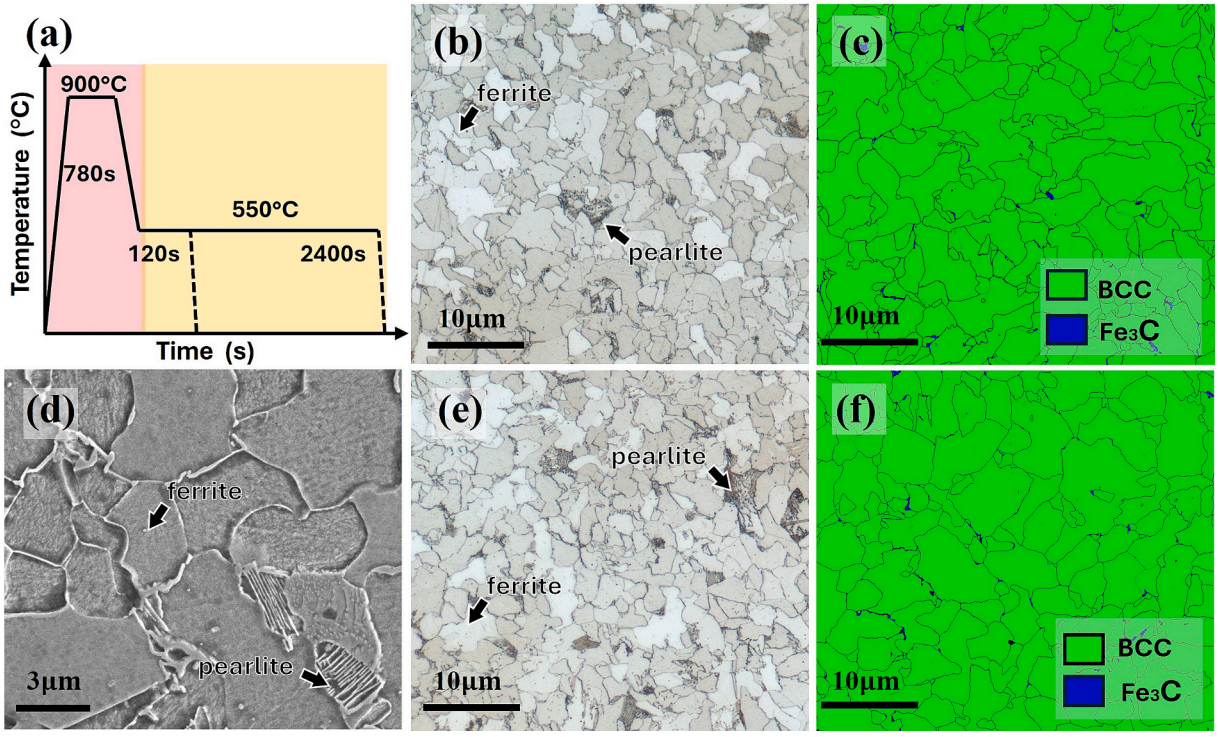

Fig. 2. Illustration of (a) the two-step heat treatment employed in this study; (b, e) optical microscopy images showing the ferrite–pearlite microstructure after aging at 550 °C for 120 s and 2400 s, respectively; (d) SEM image highlighting the morphology of ferrite and pearlite colonies; and (c, f) EBSD phase maps for 120 s and 2400 s aging, where green indicates BCC ferrite and blue denotes Fe_3C phase distribution.

Table 3
Grain size analysis of the 120 s and 2400 s using equivalent circle diameter (ECD).

Aging time (s)	Arithmetic mean (μm)	Minimum (μm)	Maximum (μm)	Standard deviation (μm)
120	4.5	1.5	13.8	1.4
2400	4.7	1.5	13.4	1.6

pearlitic matrix. In contrast, manganese exhibits a homogeneous distribution in both ferritic and pearlitic regions, as its concentration remains nearly constant in both phases. Comparison of iron and carbon contents between ferrite and pearlite, as shown in Fig. 5b, reveals a pronounced decrease in iron from approximately 96.9 at.% in ferrite to 77.1 at.% in pearlite, accompanied by an increase in carbon from about 0.12 at.% in ferrite to 21.1 at.% in pearlite due to the presence of carbon-rich Fe_3C lamellae. While the carbon content detected in the ferritic phase aligns with established carbon saturation limits, the carbon concentration in the Fe_3C phase within pearlite deviates from the ideal stoichiometry. Several factors may contribute to this deviation in the carbon content detected by APT. The analysis may be affected by background noise, while preferential evaporation or ionisation of carbon ions can lead to an underestimation of the true concentration. Furthermore, the thickness of the Fe_3C lamellae within the pearlitic microstructure introduces an additional source of error. The proximity of the pearlitic-ferrite phase can result in unintentional inclusion of ferrite within the ROI during APT reconstruction, thereby reducing the average carbon concentration owing to the substantially lower carbon content in ferrite compared with stoichiometric Fe_3C [71–73] Fig. 7Fig. 8.

In addition, carbon and nickel exhibit a tendency for segregation at ferrite–ferrite GBs, whereas copper displays distinct precipitation behaviour at these boundaries. Due to its low diffusivity in ferrite, carbon (C) segregates to the GB. Nickel (Ni) also segregates near the GB, as shown by the 1.8 at.% Ni *iso*-concentration surface in Fig. 7e. The Ni

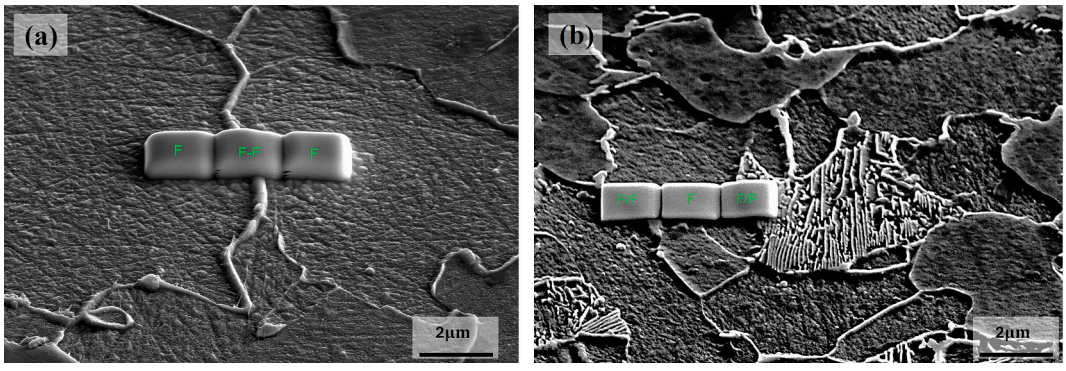

Fig. 3. SEM images showing the microstructure and APT tip lift-out locations for (a) the 120 s and (b) the 2400 s aging conditions, with selected regions corresponding to the ferrite (F) matrix, ferrite–ferrite (F-F) GBs, and ferrite–pearlite (F/P) interfaces, as marked in green.

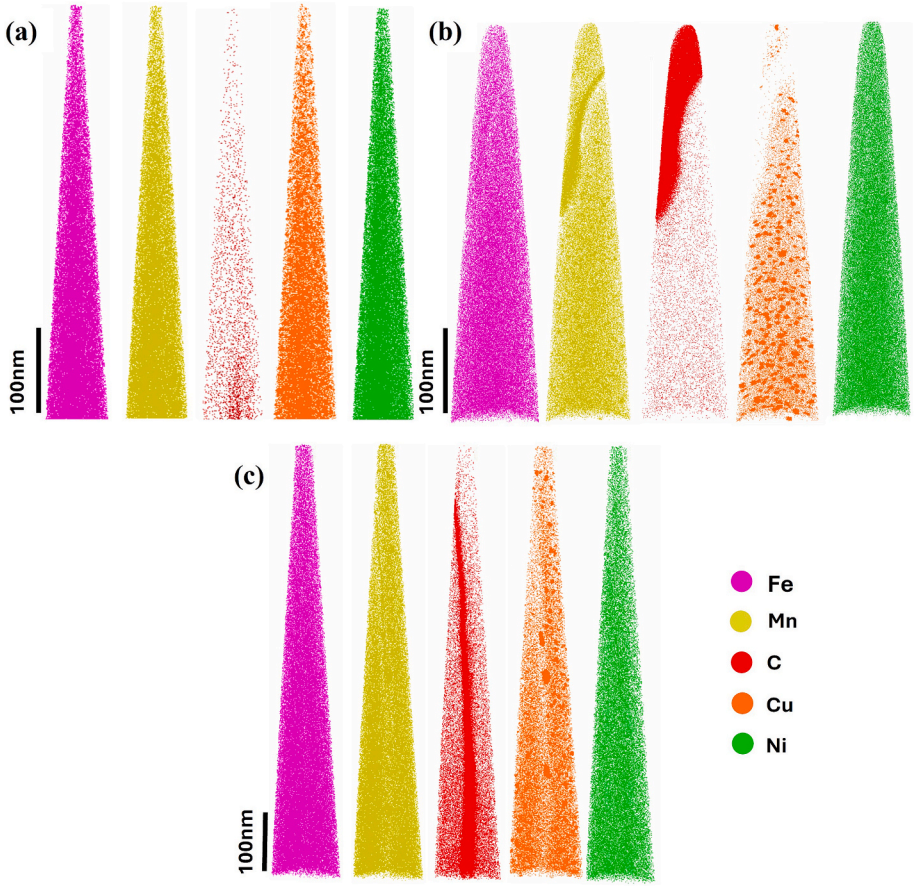

Fig. 4. Atom probe tomography maps showing the three-dimensional distribution of Fe, Mn, C, Cu, and Ni in (a) the ferrite matrix after 120 s aging, (b) a region spanning ferrite, pearlite, and their interface after 2400 s aging, and (c) the ferrite–ferrite GB after 2400 s aging, with each tip revealing the spatial partitioning and segregation of key solute elements.

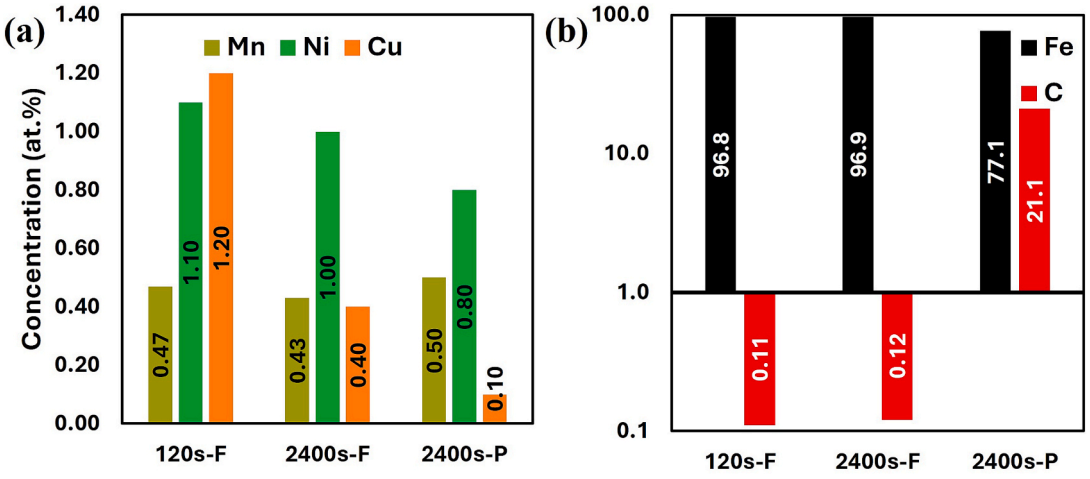

Fig. 5. Quantitative analysis of elemental concentrations in the ferritic and pearlitic regions: (a) Cu, Ni, and Mn atomic percentages measured in 120 s ferrite (120 s-F), 2400 s ferrite (2400 s-F), and 2400 s pearlite (2400 s-P); (b) comparison of Fe and C contents in the same regions, highlighting distinct compositional partitioning between matrix and pearlite regions.

segregation is likely associated, based on its spatial location, with the presence of IG Fe_3C or the Cu-$PPt_{FCC\text{-}GB}$ detected in APT and STEM analyses presented in Fig. 7 and Fig. 9. To quantify these phenomena, a detailed analysis of copper precipitation behaviour and IG carbon segregation was conducted.

3.2.2. *Precipitation evolution and GB investigation*

Due to the nature of copper precipitation kinetics, increasing the aging time influences the size, chemical composition, and lattice-structure evolution of the Cu-PPts. Fig. 6 presents the Cu-PPts visualised using the 15 at.% Cu *iso*-concentration surface in the ferritic matrix for the 120 s and 2400 s conditions, respectively. At 120 s, the precipitate diameter measured from the *iso*-concentration profiles shown in

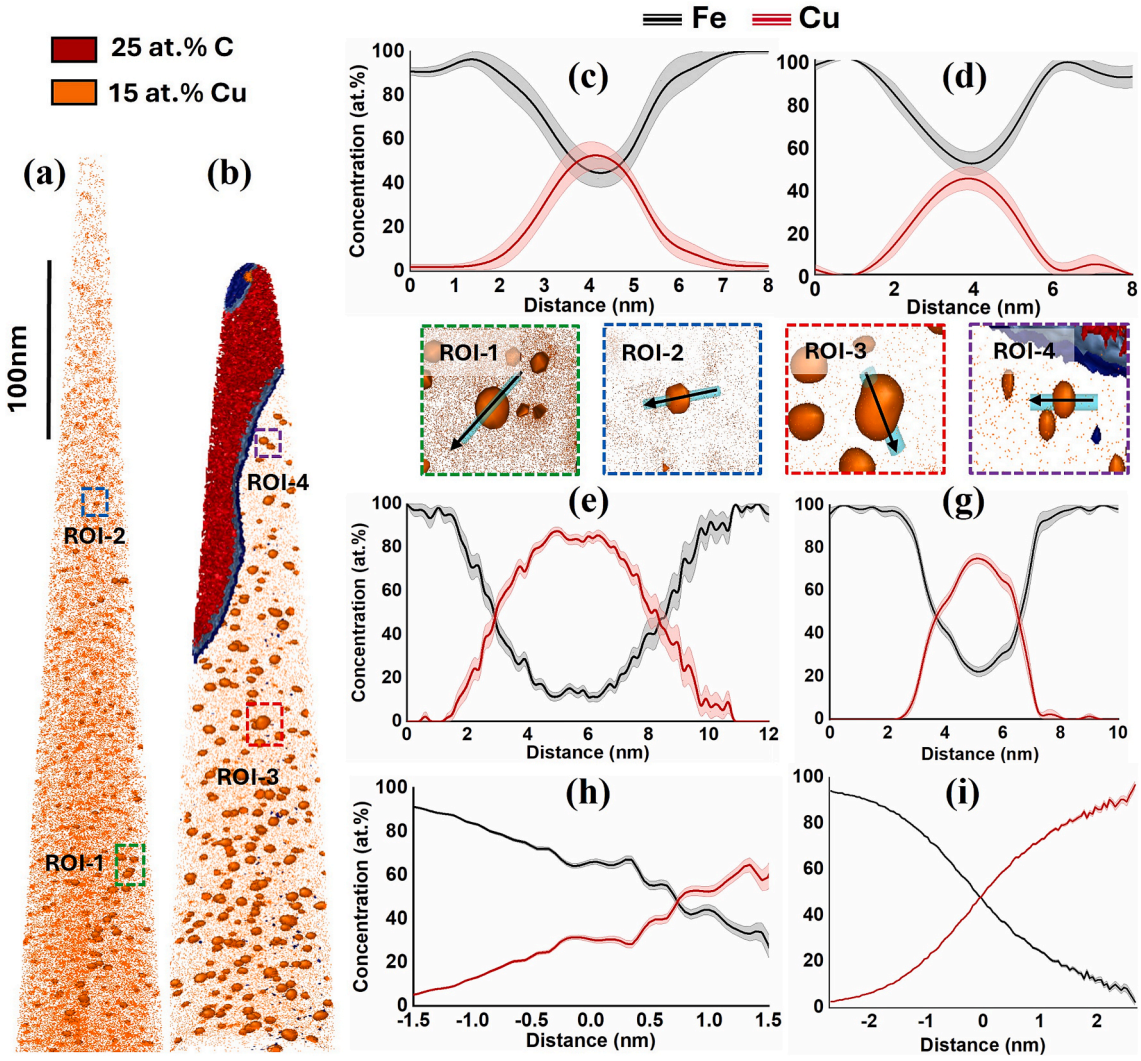

Fig. 6. APT reconstructions of the ferritic matrix shown with 15 at.% Cu *iso*-concentration surfaces highlighting Cu-PPt for (a) 120 s and (b) 2400 s aged conditions. The corresponding 1D concentration profiles of Fe (black) and Cu (red) are given for large precipitates in ROI-1 (c) and small precipitates in ROI-2 (d) for the 120 s condition, and large precipitates in ROI-3 (e) and small precipitates in ROI-4 (f) for the 2400 s condition. The proxigram concentration profiles of Cu and Fe across precipitate–matrix interfaces are shown for (h) 120 s and (i) 2400 s aging conditions.

Fig. 6.c and d ranges from approximately 2.0–4.0 nm, with the copper concentration reaching between 40 and 60 at.% within the precipitate core. Upon increasing the aging time from 120 s to 2400 s, copper diffuses from the ferritic matrix into the precipitate cores, leading to an increase in size to between 4.0 and 6.0 nm in the 2400 s condition, as shown in Fig. 6.e and, which illustrate the chemical composition of small and large precipitates, respectively Fig. 10.

The increase in precipitate size is accompanied by a corresponding rise in copper concentration, reaching up to 60–80 at.% within the precipitate core. The increase in copper concentration within the precipitates, together with a one-order-of-magnitude rise in number density (as summarised in Table 4), explains the observed decrease in matrix copper content, as previously discussed and shown in Fig. 5. The copper depletion in the matrix results from both the nucleation of new Cu-PPt_{BCC} precipitates and the growth-induced structural transformation of existing Cu-PPt_{BCC} into Cu-PPt_{9R}, which consumes copper from the surrounding matrix. These mechanisms are consistent with the number density increase and the precipitation sequence simulated by the MatCalc as illustrated in Fig. 11. Specifically, the 2400 s condition reflects the concurrent nucleation of Cu-PPt_{BCC} and the growth and transformation of older precipitates into Cu-PPt_{9R}, as shown in Fig. 11.b, leading to an increased volume fraction from 0.0015 at 120 s to 0.0085 at 2400 s. The size evolution and copper enrichment within the precipitates further support this transformation, in agreement with the simulation results across the extended aging period from 120 s to 2400 s.

To assess the elemental segregation and copper precipitation at the GB (clearly visible in the videos attached to Fig. S2. of the supplementary materials), the *iso*-concentration surfaces of 1.8 at.% Ni, 0.8 at.% Mn, 3 at.% C and 15 at.% Cu are used as displayed in Fig. 7.a,d, and e. The *iso*-concentration surfaces reveal pronounced IG carbon enrichment accompanied by disc-shaped Cu-PPts distributed along the GB, which are markedly larger than the rounded Cu-PPts observed within the matrix. The one-dimensional (1D) concentration profiles illustrated in Fig. 7.b and c, constructed using ROI-1 and ROI-2, which go through the IG Cu-PPts and the matrix precipitates respectively, show that while the large disc-shaped Cu-PPt at the GB has a copper concentration of nearly 100 at.% in its core, the copper concentration in the core of the matrix precipitates are nearly 80 at.%. Nonetheless, while the matrix Cu-PPts have an average diameter of about 5 nm, the disc-shaped Cu-PPt found at the GB exhibits a minor diameter (thickness) of approximately 10 nm and a major diameter of approximately 50 nm.

The distinct increase in copper content and the size of the IG Cu-PPts are consistent with the typical dimensions associated with Cu-PPt_{FCC} and with the MatCalc simulation of IG −$PPt_{FCC\text{-}GB}$ formed in association

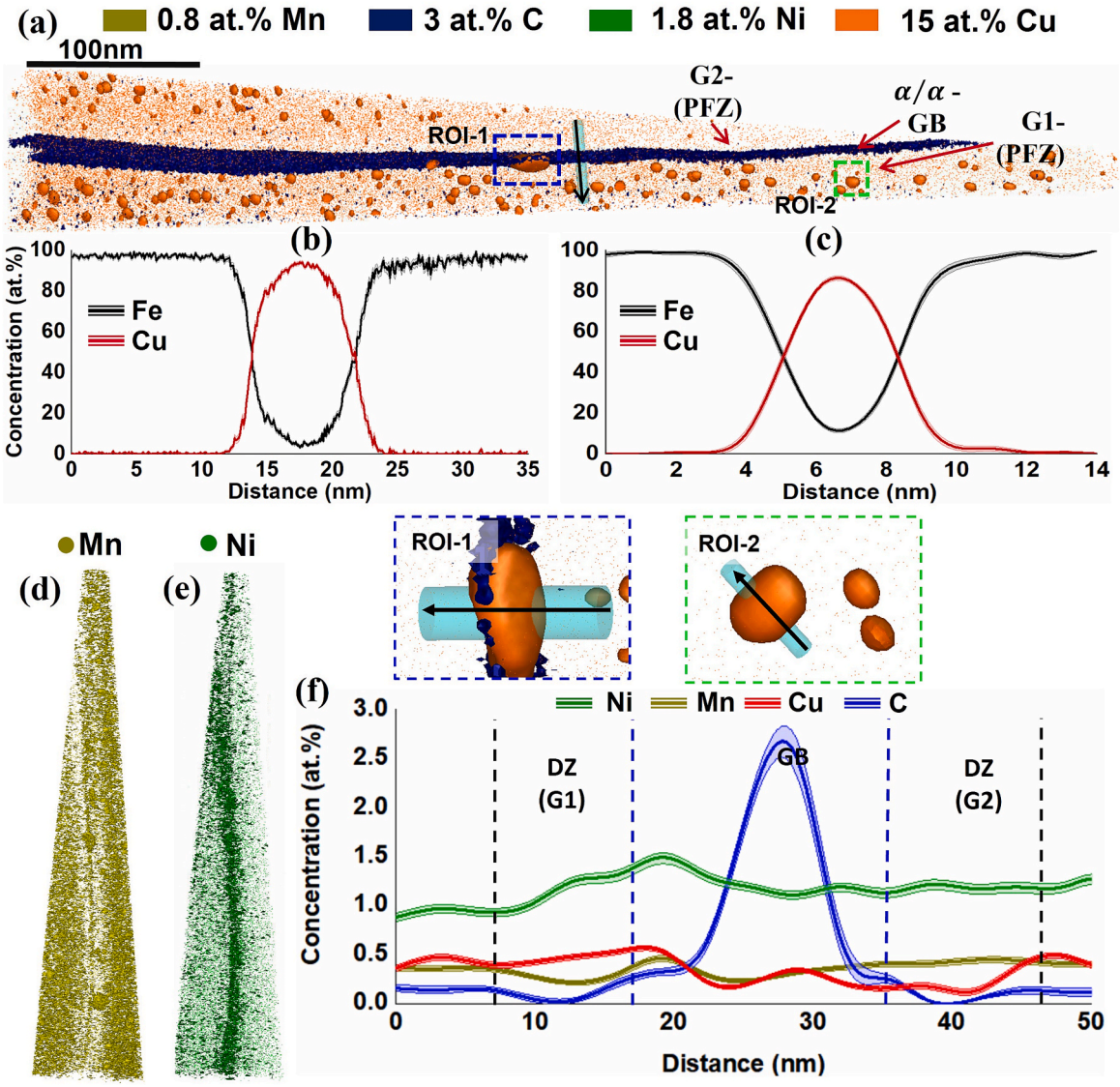

Fig. 7. APT reconstruction of the 2400 s-aged condition showing (a) a C-enriched GB decorated by IG disc-shaped Cu-PPts, visualized using 3 at.% C and 15 at.% Cu isoconcentration surfaces; (b) and (c) illustrate the difference between an IG disc-shaped Cu-PPt$_{FCC\text{-}GB}$ and Cu-PPt$_{9R}$ in the matrix; (d) and (e) show Mn and Ni segregation to the GB, respectively; (f) presents a 1D concentration profile across the GB ROI, depicting the localized chemical composition and elemental partitioning.

with Fe_3C and carbon enrichment. According to the MatCalc simulation results presented in Fig. 11, the IG Cu-PPt is expected to have transformed into Cu-PPt$_{FCC\text{-}GB}$ during cooling, prior to the onset of aging, as the elevated temperature and IG location promote an accelerated transformation from Cu-PPt$_{BCC}$ to Cu-PPt$_{FCC}$.

Due to their position at the GBs, which serve as preferential and accelerated diffusion paths, the Cu-PPts exhibit evidence of both bulk and GB-assisted diffusion, leading to the pronounced growth of Cu-PPt$_{FCC\text{-}GB}$.

The effects of IG carbon enrichment, and Cu, Ni, and Mn segregation at the GB were further examined using a 1D concentration profile generated along a region-of-interest (ROI) cylinder traversing the ferrite-ferrite GB, as illustrated in Fig. 7a. The 1D concentration profile shown in Fig. 7f reveals a lower copper concentration surrounding the GB compared with the adjacent matrix. Within the ferritic matrix (G2), the copper concentration decreases, forming a DZ with less than 0.2 at.% Cu, compared to an average of approximately 0.4 at.% in the matrix. Additionally, a PFZ forms near the GB – particularly pronounced in the second grain (G2) – where minimal or no copper precipitation is detected. Similar to copper, the carbon concentration in the matrix is approximately 0.12 at.%, but it drops to about 0.02 at.% on both sides of the GB. The combined C and Cu depletion and the presence of a PFZ are further corroborated by the APT heat maps shown in Fig. S3 of the supplementary materials.

In contrast, the GB itself exhibits significant carbon enrichment, reaching nearly 3 at.%. This enrichment stands in sharp contrast to the pronounced carbon depletion in the adjacent regions on both sides of the boundary. Likewise, Mn and Ni show distinct segregation behaviour at the GB. While Ni segregates near the boundary shown in Fig. 7e, its concentration increases from approximately 1 at.% in the matrix to about 1.5 at.% at the GB. Mn, on the other hand, displays the opposite trend. As seen in Fig. 7d, its content decreases from roughly 0.5 at.% in the matrix to 0.25–0.30 at.% within the DZ surrounding the GB, before rising again to around 0.6 at.% directly at the boundary. The segregation of Mn and Ni at the GB is potentially correlated with the presence of IG Fe_3C and the Cu-PPt$_{FCC\text{-}GB}$ phase, and their concurrent formation. As C and Cu atoms diffuse towards the IG Fe_3C and Cu-PPt$_{FCC\text{-}GB}$, Ni and Mn are rejected from the growing IG Fe_3C and Cu-PPt$_{FCC\text{-}GB}$, producing the observed segregation profiles.

The formation of the Cu- and C-DZ, marked by the orange colour in

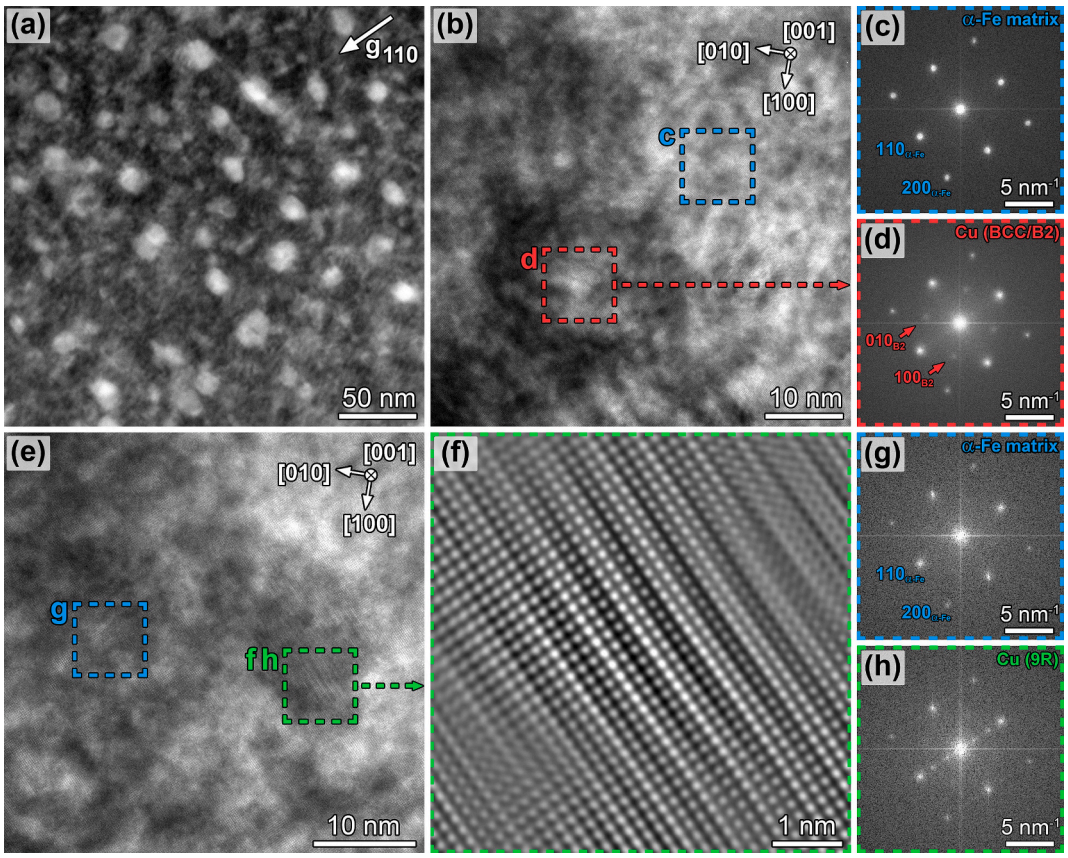

Fig. 8. (a) Overview showing the characteristic distribution of Cu-rich precipitates in the α-Fe matrix (120 s condition) using two-beam LAADF-STEM DCI condition with diffraction vector g = [110] and electron beam close to [001] zone axis of the α-Fe BCC matrix. (b) HR-TEM detail of coherent Cu-rich nanoprecipitate and corresponding FFT diffraction patterns are taken from the α-Fe BCC matrix (region c) and the Cu-rich precipitate (region d) with notable superlattice reflections indicating BCC–B2 crystal structure (120 s condition). (e) Detail from 2400 s condition showing Cu-rich precipitate exhibiting (f) Moiré-like fringe contrast in HR-TEM, indicating 9R crystal structure. Corresponding FFT diffraction patterns taken from the α-Fe BCC matrix (region g) and the Cu-rich precipitate (region h). For (b-h), the electron beam is parallel to the [0 0 1] zone axis of the α-Fe BCC matrix.

Fig. 7f, results from the formation of a C-enriched layer and large Cu-PPts at the GB, marked by the red colour in the same figure. These features consume the C and Cu atoms from the surrounding matrix and leave behind a PFZ, as can be seen in Fig. 7. The implications of IG carbon enrichment and copper precipitation for GB strength are examined in detail in the Discussion section.

3.3. Scanning transmission electron microscopy (STEM)

The presence of C-enriched GBs, as depicted in Fig. 7, is also correlated with the preferred nucleation sites of IG Fe_3C [74]. To investigate the possible presence of Fe_3C at these C-enriched GBs, as well as to examine the evolution of copper precipitation and the crystal lattice structure of copper in both the matrix and GBs at different aging times, a detailed multi-scale S/TEM-based characterisation was performed on the matrix and ferrite–ferrite GBs in both the 120 s and 2400 s specimens.

Using the LAADF-STEM DCI technique under two-beam approximation, Fig. 8.a presents the characteristic distribution of Cu-PPts in the α-Fe BCC matrix for the 120 s condition. High-resolution details of the copper precipitate are revealed in Fig. 8.b using HR-TEM. Comparison of the corresponding FFT diffraction patterns taken from the α-Fe BCC matrix (Fig. 8.c) and the Cu-rich precipitate (Fig. 8.d) clearly confirms cubic crystal structures for both the α-Fe BCC matrix and the Cu-rich precipitate, and further suggests a coherent cube-on-cube orientation relationship (OR) between the two lattices. Moreover, the FFT diffraction pattern obtained from the Cu-PPt exhibits notable superlattice reflections, which clearly indicate an ordered BCC–B2 crystal structure. The presence of such a superlattice diffraction pattern has been reported specifically for the ordered B2 Cu-PPt_{BCC}, arising from differences in scattering amplitudes between Fe and Cu atoms. This phenomenon occurs when the Fe:Cu ratio in the Cu-PPts approaches 1:1, consistent with findings in the literature and with the APT analysis of the 120 s sample, showing Cu concentrations in the precipitate cores ranging between 40 and 60 at.% and Fe concentrations between 60 and 40 at.% [40,41,75].

The increase in Cu content within the Cu-PPts or clusters with further coarsening leads to greater structural disorder within the precipitates. According to earlier studies [42], this occurs as more Cu atoms progressively replace the Fe atoms on the $\{110\}_{B2}$, resulting in an increased copper concentration within the precipitate core. This observation is consistent with the experimentally observed rise in copper content within Cu-PPts when comparing the precipitates at 120 s and 2400 s conditions, as shown in Fig. 6.

The free energy generated by the weakened order in the BCC Cu phase and the compressive stresses acting on the Cu-PPt_{BCC} becomes sufficiently high to induce a martensitic transformation into Cu-PPt_{9R} [40,76]. Using HR-TEM imaging, Fig. 8e shows the area containing the Cu-rich precipitate in the 2400 s condition. The FFT diffraction pattern taken from the matrix (highlighted by a blue dashed rectangle, detail in Fig. 8g) confirms the BCC crystal structure of the α-Fe matrix. The FFT-filtered HR-TEM micrograph in Fig. 8f reveals the crystal structure of the Cu-rich precipitate in detail, showing a distinctive Moiré-like fringe pattern occurring every three atomic column planes along the [001] zone-axis viewing direction. This effect is associated with the fact that the coarsened Cu-rich precipitates in 2400 s condition do not have an ordered cubic crystal structure anymore. Instead, both HR-TEM (Fig. 8f)

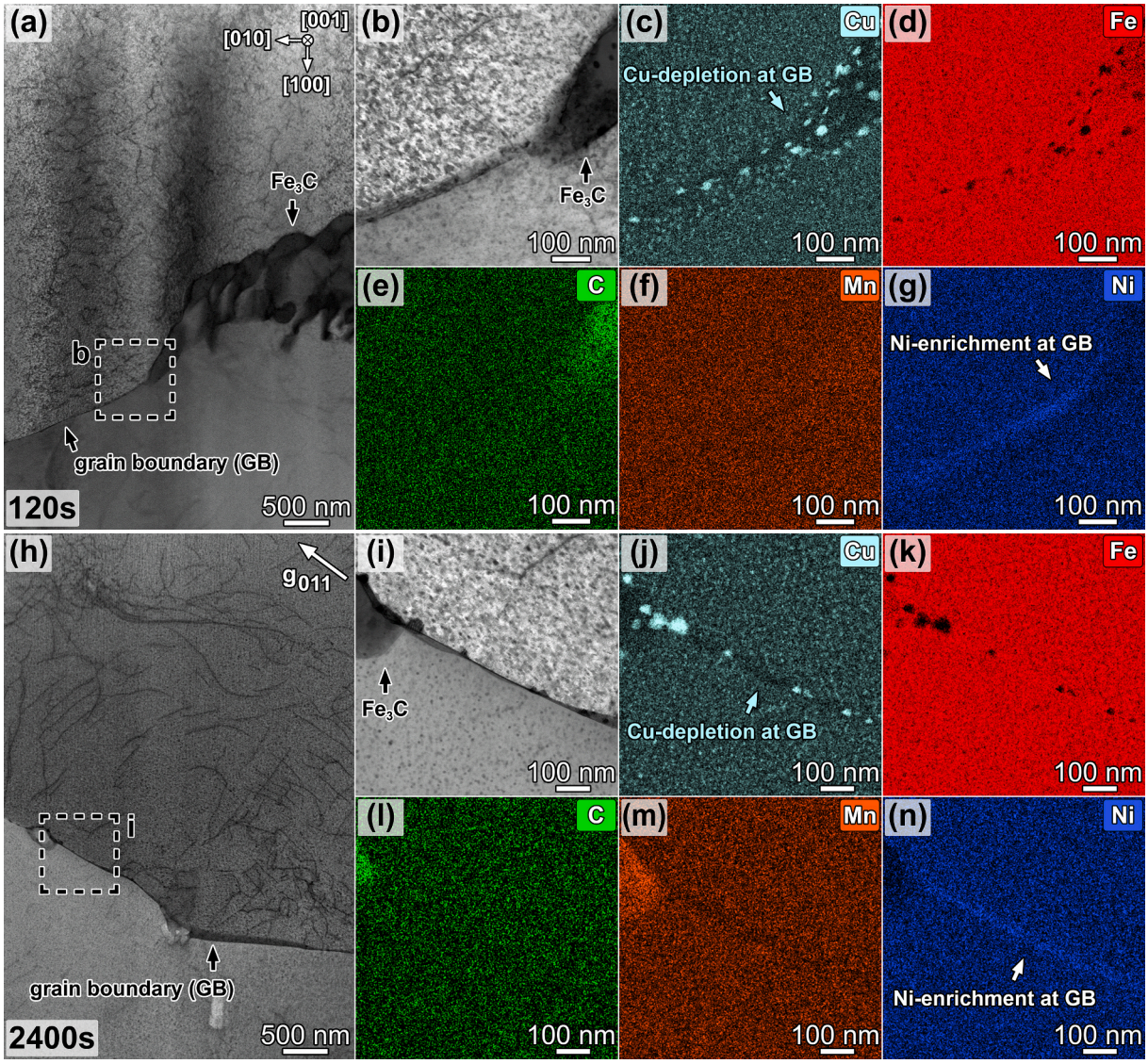

Fig. 9. A) overview of characteristic gb area for condition "120 s" is shown using BF-STEM DCI with electron beam parallel to [001] zone axis of the α-Fe grain on the top. (b) Detail of the GB near Fe3C as highlighted by a black dashed rectangle in (a). Corresponding STEM-EDS elemental maps are shown in (c-g). (h) BF-STEM DCI showing typical GB area for condition "2400 s", electron beam close to [001] zone axis of the α-Fe grain on the top. (i) Detail of the GB near Fe_3C as highlighted by a black dashed rectangle in (h). Corresponding STEM-EDS elemental maps are shown in (j-n). In both conditions, notably coarsened Cu-PPts, and the elemental Cu-depletion/Ni-enrichment are observed at the GBs.

and the associated FFT diffraction pattern (Fig. 8h) indicate the presence of a stacking sequence characteristic of the 9R-type crystal structure, in which the sequence of close-packed planes (ABCBCACAB) repeats every third layer. This observation is in excellent agreement with similar results reported for Cu-rich precipitates in [40].

It is important to note that the defect-free FCC equilibrium crystal structure of Cu is more energetically favourable than the 9R structure; hence, with increasing aging time or accelerated diffusion from the surrounding ferritic matrix toward the Cu-PPts, the 9R precipitates eventually transform into the FCC lattice structure, as discussed later for larger precipitates at GBs. Overall, the STEM and HR-TEM analyses demonstrate that copper precipitation in the matrix begins with ordered B2 Cu-PPt_{BCC} in the 120 s condition and evolves into Cu-PPt_{9R} as the aging time increases to 2400 s. This result is in excellent agreement with the APT analyses and MatCalc simulations of precipitation behaviour.

The STEM characterisation of areas surrounding the GBs confirms the presence of high C concentrations at the boundaries and significantly larger Cu-PPts than those found in the matrix, as shown in Fig. 9a–b, and Fig. 9h–i for the 120 s and 2400 s conditions, respectively. The corresponding STEM-EDS elemental composition maps further reveal that, in regions containing large Cu-PPts, the particles are predominantly depleted in Fe, as clearly observed in Fig. 9.d and k. This result is consistent with the APT analysis of the Cu-PPt_{GB}, which shows a chemical composition of more than 95 at.% Cu and approximately 5 at.% Fe.

The large Cu-PPts are detected exclusively at ferrite–ferrite GBs and within IG Fe_3C. Additionally, the STEM-EDS maps confirm Ni segregation, as well as Mn and Cu depletion, in the vicinity of the GB – consistent with APT results (see Fig. 7). The carbon depletion could not be detected using the STEM-EDS maps because of the inherent limitations of EDS in detecting and quantifying light elements, particularly when C depletion of only a few at.% occurs in multi-component systems [77,78]. The size of the Cu-PPts at the ferrite-ferrite GBs detected by APT matches both the size and chemical composition of the FCC Cu-PPts characterised by STEM. The micrographs documenting IG carbon enrichment at ferrite–ferrite GBs with large Cu-PPts after aging for 120 s and 2400 s are shown in Fig. 9a and h. The STEM-EDS elemental maps from regions around the GBs indicate that the Cu-PPts consist

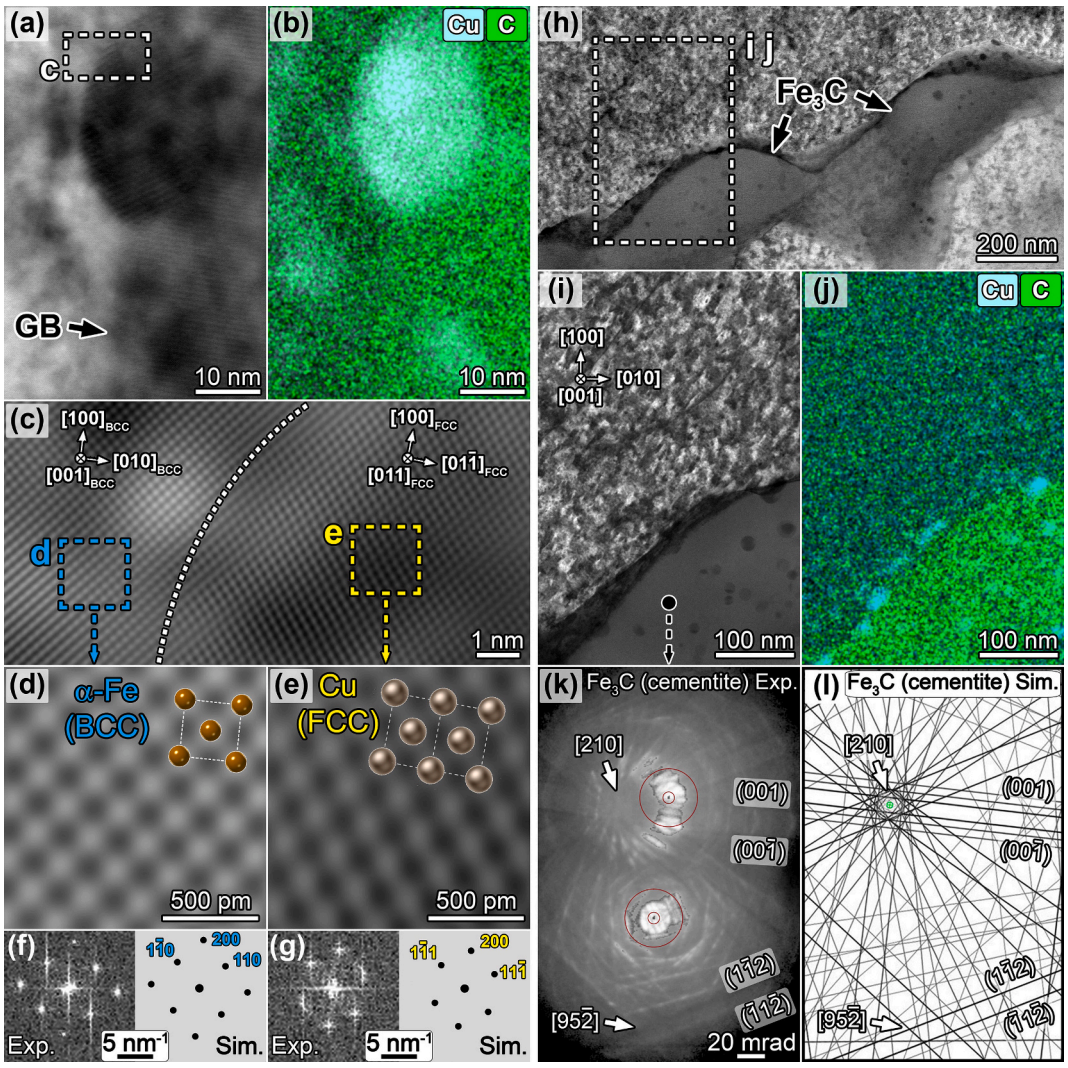

Fig. 10. (a) BF-STEM image of coarsened Cu-PPts at the GB and (b) corresponding STEM-EDS maps of Cu and C from the same area. (c) FFT-filtered HAADF-STEM image showing detail of the interface between (d) the α-Fe BCC matrix and (e) the Cu-PPt. Experimentally obtained STEM images and corresponding experimental and simulated FFT diffraction patterns confirm the N–W OR between (f) α-Fe BCC matrix and (g) the Cu-PPt$_{FCC}$. Unit cells of both crystal lattices in (d) and (e), as well as diffraction patterns in (f) and (g), were simulated using Crystal Maker Suite software. (h) BF-STEM image of Fe_3C precipitates at the GB between two α-Fe BCC grains. (i) Detail of the interface between the α-Fe BCC matrix and Fe_3C, and (j) corresponding STEM-EDS maps of Cu and C from the same area. Comparison of (k) experimentally obtained and (l) simulated CBED/Kikuchi patterns confirms the orthorhombic crystal structure of the Fe_3C. The electron beam was parallel to the [0 0 1] zone axis of the α-Fe matrix in (a-j).

Table 4
Precipitate size, number density, and copper content evolution with increasing aging time.

Aging time (s)	Mean diameter (nm)	Number density (m^{-3})	Average copper content (at.%)	Volume fraction (%)
120	3.0	6.7×10^{22}	40–60	0.0015
2400	5.0	1.3×10^{23}	60–80	0.0085

exclusively of copper and lack nickel or manganese contributions (see also the STEM-EDS compositional line profiles from the Cu-PPt in Fig. S4 of the Supplementary Materials). That is fully in agreement with the chemical composition measured by APT based on the 1D concentration profiles in Fig. 6. Although the high carbon segregation detected in Fig. 10 indicates the presence of a Fe_3C phase, and the chemical composition and size of Cu-PPt$_{GB}$ at the IG Fe_3C and GB– determined through APT in Fig. 7– indicate an FCC lattice structure, experimental confirmation through simulations was required. Therefore, Crystal Maker Suite software was used to simulate the diffraction of the IG C-enriched phase and the Cu-PPt$_{GB}$.

An interface containing the C-enriched phase lying between two ferrite grains and hosting large Cu-PPt$_{GB}$ was investigated. BF-STEM micrograph in Fig. 10.a shows coarsened Cu-PPt at the GB as confirmed by the corresponding STEM-EDS map of Cu and C from the same area (Fig. 10b). FFT-filtered HAADF-STEM image (Fig. 10c) reveals the detail of the interface between the α-Fe BCC matrix (Fig. 10d) and Cu-PPt$_{FCC\text{-}GB}$ (Fig. 10e). Experimentally obtained STEM images and corresponding experimental and simulated FFT diffraction patterns are consistent with the Nishiyama–Wasserman (N–W) OR [54,71–73] between the α-Fe BCC matrix (Fig. 10f) and the large disc-shaped Cu-PPt$_{FCC\text{-}GB}$ at the GB (FCC, Fig. 10g), where $[001]_{BCC} \| [011]_{FCC}$, and $(1\bar{1}0)_{BCC} \| (1\bar{1}1)_{FCC}$. Unit cells of both crystal lattices (Fig. 10d-e) as well as diffraction patterns (Fig. 10f-g) were simulated using Crystal Maker Suite software. Different example in Fig. 10h documents the Fe_3C phase at GB between two α-Fe grains using BF-STEM. Details of the interface between the α-Fe BCC matrix and Fe_3C and corresponding STEM-EDS maps of Cu and C from the same area are shown in Fig. 10i and j,

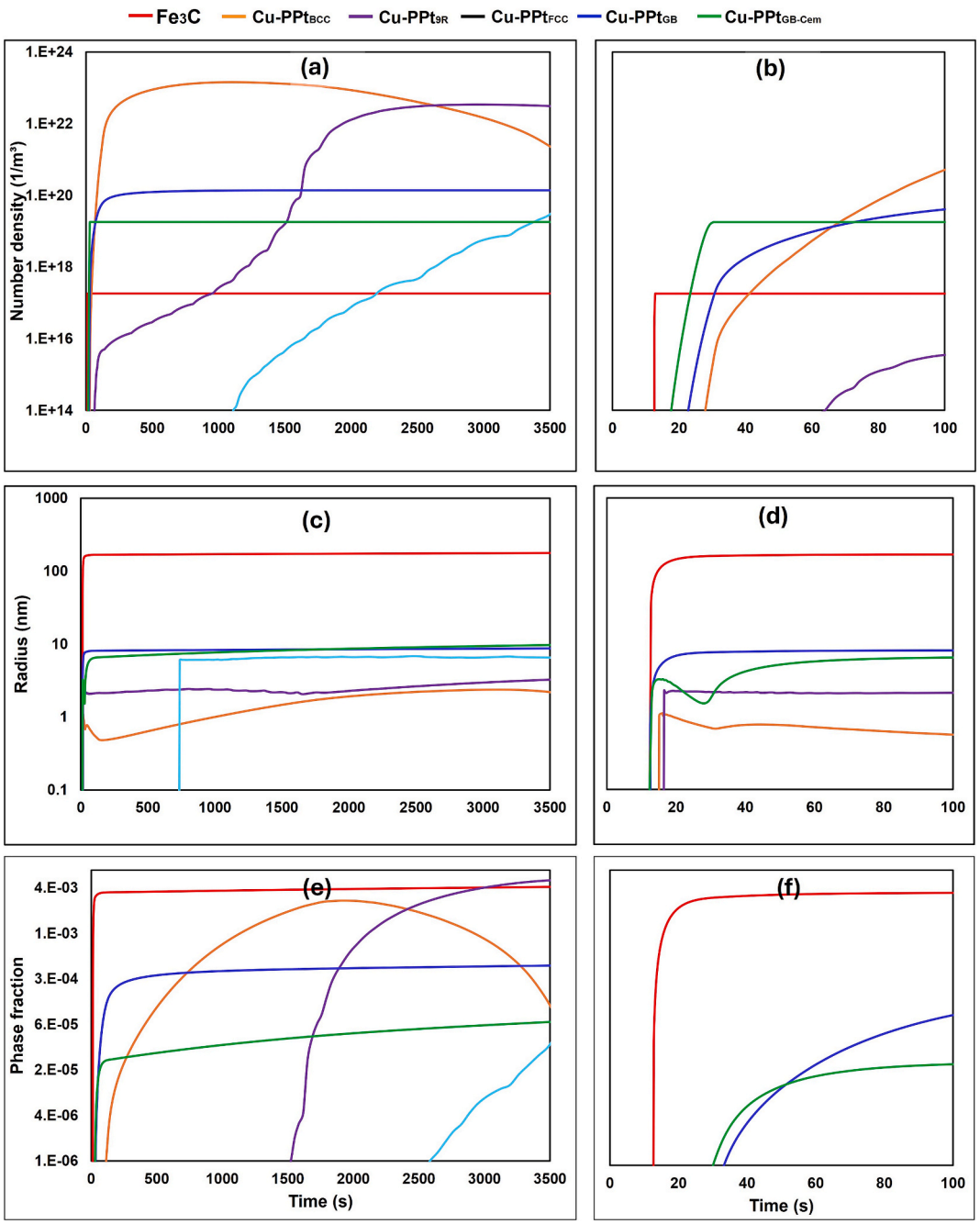

Fig. 11. MatCalc Precipitation-kinetic simulation showing the evolution of (a) Number density, (c) mean radius, and (e) phase fraction evolution. Subplots (b), (d), and (f) present zoomed-in views of the initial stages corresponding to (a), (c), and (e), respectively, to highlight the early growth behaviour of each precipitate type.

respectively.

The orthorhombic crystal structure of the Fe_3C is confirmed by comparison of experimentally obtained (Fig. 10k) and simulated convergent beam electron diffraction (CBED)/Kikuchi patterns in reciprocal space (Fig. 10l).

Multi-scale electron microscopy complemented by Crystal Maker Suite software simulation results collectively confirm the formation of IG Fe_3C along ferrite–ferrite GBs/interfaces. These IG Fe_3C and C-enriched GBs act as preferential sites for Cu-PPt_{GB} formation, serving as diffusion pathways that enable accelerated Cu-$PPt_{FCC\text{-}GB}$ precipitation during cooling or early stages of aging. This process, which typically requires thousands of seconds to occur in the matrix during isothermal aging, is significantly expedited at the GBs. Thus, the STEM observations are fully consistent with the APT results, validating the proposed mechanism of IG Fe_3C formation and disc-shaped Cu-PPt_{GB} precipitation.

3.4. Precipitation simulation kinetics

The simulated evolution of the precipitation phase fractions, number densities, and mean radius during the cooling from 900 °C (initial 130 s) and subsequent isothermal holding at 550 °C are shown in Fig. 11. Precipitation nucleation started already during the cooling period, but only after ferrite formation (below 790 °C). Fe_3C nucleation is completed almost instantaneously (within 1 s), and the precipitates reach the size equivalent to a sphere mean radius of roughly 180 nm, which is interpreted in terms of lamella thickness of about 8 nm and diameter of about 2 μm. The molar phase fraction increases during the

simulated time of the isothermal stage by about 17% (from 0.0036 to 0.0042). Cu-PPts nucleation on these Fe_3C precipitates is completed above 630 °C. These Cu-$PPt_{FCC\text{-}Cem}$ nuclei reach the mean radius of 5 nm at the onset of the isothermal holding and increase further in size therein, reaching the radius of 9 nm.

Nucleation of Cu-PPts on the GBs (Cu-$PPt_{FCC\text{-}GB}$ and Cu-$PPt_{FCC\text{-}Cem}$) is almost halfway completed during the cooling time, reaching the number density around $6.4 \times 10^{19} m^{-3}$. A further increase towards $1.4 \times 10^{20} m^{-3}$ occurred during the isothermal holding, and the final mean radius of 9 nm was calculated. The comparison of number densities between Cu-$PPt_{FCC\text{-}GB}$ and Cu-$PPt_{FCC\text{-}Cem}$ yields the ratio of about 8:1. Nucleation of Cu-BCC clusters in the ferrite grains starts already during the cooling, but the most nuclei form during the isothermal stage. This can be clearly seen when comparing the number density value of $4 \times 10^{21} m^{-3}$ at the start of this step with the one after 1000 s ($1.4 \times 10^{23} m^{-3}$). At the simulation end, the number density of Cu-PPt_{BCC} declines towards $6.6 \times 10^{20} m^{-3}$ due to the coalescence of the smaller clusters and transformation towards Cu-PPt_{9R} of the larger ones.

The switch between these two regimes is assumed to be around 1800 s of holding time, when Cu-PPt_{BCC} phase fraction reaches the maximal value of 0.0028. Past this moment, the phase fraction decrease is accompanied by the increase of Cu-PPt_{9R} phase fraction value, and the mean cluster radius stabilizes around a 2 nm range, assumed as the lower size limit for the Cu-PPt_{BCC} → Cu-PPt_{9R} transformation.

While the simulation shows the presence of the first Cu-PPt_{9R} precipitates at the end of the cooling period, the calculated number density of $4.9 \times 10^{15} m^{-3}$ and the mean size in the nanometer range for this precipitate does not allow for any experimental verification of this result. With an increasing number of Cu BCC-clusters reaching transformation size, the number density of Cu-PPt_{9R} rises to $2.6 \times 10^{22} m^{-3}$ at the simulation end, surpassing the number density of Cu-PPt_{BCC}. After 1500 s of holding stage, an increase of Cu-PPt_{9R} phase fraction is observed, reaching the value of 0.0053 at the simulation end. The mean radius of the Cu-PPt_{9R} precipitates at the simulation end stays in the range of 3 nm. Transformation towards the first Cu-PPt_{FCC} precipitates is predicted after 400 s.

4. Discussion

The investigation conducted in this study reveals a distinct and accelerated IG copper precipitation mechanism occurring at C- enriched GBs and IG Fe_3C associated with a nanosized PFZ. Understanding the presence of IG Fe_3C and Cu-PPts provides insights into the IG crack initiation behaviour of medium-carbon copper-alloyed ferritic steel under fatigue conditions [33,35]. The Cu-PPts found explicitly in the ferrite matrix differ significantly from those precipitating at the GBs with regard to their size, chemical composition, and lattice structure. Those differences, in addition to the potential evolution mechanism of the IG carbon enrichment/Fe_3C and Cu-PPts, are discussed and linked to their effect on GB chemistry and strength, and how they influence the IG crack initiation behavior.

4.1. Evolution of copper precipitation in the matrix

Cu-PPts were found to form exclusively within the ferritic matrix. Upon increasing the aging time, the Cu-PPt followed the well-established crystallographic transformation sequence [44]. The FFT diffraction patterns from STEM analysis revealed (i) the initial coherent Cu-PPt_{BCC}, indicated by the presence of superlattice reflections; (ii) the subsequent precipitate growth accompanied by a gradual loss of coherency, reflected by the disappearance of the superlattice pattern; and finally, (iii) the martensitic transformation into the 9R structure, as identified through FFT diffraction patterns in combination with HR-TEM imaging. Here, the characteristic untwinned 9R structure manifests itself through a change in the stacking sequence of the close-packed planes (ABCBCACAB) [45]. The Cu-PPts transformation sequence corresponds to the observed size evolution from an average radius of 2–3 nm in the BCC condition to 4–5 nm in the 9R condition. [8,44,45,49]. The increase in precipitate size is accompanied by a substantial enrichment of copper within the precipitate core and a corresponding depletion of copper in the surrounding ferritic matrix. This is particularly evident when comparing the copper content in the 120 s ferritic matrix with that in the 2400 s matrix, where the Cu concentration decreases from approximately 1.2 at.% to 0.4 at.%, according to APT. This reduction in matrix Cu content arises not only from precipitate growth and transformation, which require diffusion of Cu from the matrix into the precipitates [12,13,48], but also due to the ongoing nucleation of new Cu-PPt_{BCC} that occurs concurrently with the growth of existing Cu-PPts at 2400 s.

Kinetic simulation results reproduce the experimentally observed formation of BCC clusters and their subsequent transformation toward the 9R structure. Simulated number densities are within an order-of-magnitude range of the APT results ($3.5 \times 10^{22} m^{-3}$ for 120 s, $6.8 \times 10^{22} m^{-3}$ for 2400 s). Simulated number density peak value is observed at 950 s of isothermal holding, which suggests that the nucleation at 120 s is not yet completed. On the contrary, at 2400 s, the decreasing number density of BCC clusters ($3.8 \times 10^{22} m^{-3}$) is almost equal to the one of 9R-phase ($3 \times 10^{22} m^{-3}$) indicating the ongoing transformation process. This observation is in line with the detection of the 9R phase in the respective sample. Simulated BCC-cluster size for 120 s (mean diameter of 1 nm) is smaller than the measured clusters, while the one for 2400 s (mean diameters are approximately 3 nm for BCC and 5 nm for 9R) matches the observed values well. The simulated BCC-cluster size for 120 s (mean diameter ≈ 1 nm) is smaller than the experimentally measured clusters, whereas the simulated sizes for 2400 s (mean diameters of approximately 3 nm for BCC clusters and 5 nm for the 9R phase) agree well with the observed values. The discrepancy at 120 s may be explained by the limited detectability of very small clusters in APT measurements, as clusters with very small diameters are typically underrepresented, and the analysis preferentially captures larger precipitates. Finally, Cu-PPt_{FCC} are not expected at 120 s, and the predicted number density value of about $1 \times 10^{18} m^{-3}$ at 2400 s condition remains well below the detection limit of the APT method.

4.2. Evolution of copper precipitates at the ferrite GB

The Cu-PPts observed at ferrite GBs exhibit distinct characteristics – particularly in size, distribution, and lattice structure – compared with those within the ferritic matrix. These differences are attributed to the influence of IG carbon enrichment and the presence of IG Fe_3C, at which the Cu-PPts nucleate.

The formation of IG Fe_3C and Cu-PPts may occur either simultaneously or sequentially during the austenite–ferrite decomposition, either as interphase precipitation upon cooling from 900 °C to 550 °C or as IG precipitation during the aging stage at 550 °C [54,55,79,80]. In this study, we hypothesise that, following the formation of C-enriched GBs and IG Fe3C, the IG Cu-PPts form successively. Specifically, Fe_3C precipitation occurs during the austenite–ferrite decomposition, leading to the formation of an interphase Fe_3C layer. Subsequently, nuclei of disc-shaped Cu-$PPt_{FCC\text{-}GB}$ form during the later stages of the austenite–ferrite decomposition, during cooling and prior to the onset of aging, using the IG Fe_3C and the ferrite–ferrite C-enriched GB as preferred and accelerated nucleation paths.

Upon cooling from the austenitisation temperature range, the low solubility of carbon in the ferritic matrix of approximately 0.022 wt% [81] forces carbon atoms to diffuse from ferrite toward the moving interphase boundary, eventually leading to the formation of an IG Fe_3C layer at the ferrite–ferrite GB, as revealed by the APT and STEM analyses. The shape and location of the IG Fe_3C phases situated between ferrite grains provide strong morphological evidence–supported by both experimental and atomistic studies–that these Fe_3C layers originate from

the austenite–ferrite transformation and maintain an OR with the interphase boundary [82,83], unlike the Fe_3C or carbides forming independently of austenite decomposition usually found in discrete spherical morphologies inside the matrix. This precipitation behaviour is also consistent with the mechanism described by Morsdorf, where Fe_3C forms during quenching from the Austenitisation temperature range [74].

Although IG copper precipitation can form either as a result of austenite transformation or during subsequent aging, the morphological and spatial characteristics of the precipitates are distinct, providing insight into their formation mechanism. Cu-PPt formed during austenite decomposition – particularly via interphase precipitation or at the migrating austenite/ferrite interface – typically exhibit disc-shaped or elliptical morphologies and are arranged in periodic rows or sheets parallel to the transformation front or GBs. This arrangement arises directly from repeated nucleation events at the moving interface and has been documented in both classical and contemporary studies [8,9,54,79,80]. These precipitates are intimately associated with the transformation interface and frequently display a crystallographic OR with the parent phase, serving as a microstructural signature of transformation-induced precipitation [17,55,84].

In contrast, Cu-PPts formed during isothermal aging – such as tempering or extended holding after transformation – are generally distributed more randomly within the matrix or along GBs, lacking any defined alignment or periodic arrangement [17,55,84]. These aging-induced precipitates tend to be spherical or ellipsoidal, and their size and distribution are governed by aging temperature and time, rather than by the dynamics of a transformation front. Thus, the presence of disc- or elliptical-shaped Cu-PPts arranged in rows or sheets along GBs is characteristic of precipitation occurring during austenite transformation, whereas randomly distributed, spheroidal precipitates are characteristic of isothermal aging. This distinction is consistently corroborated by detailed TEM and microstructural analyses reported across the cited literature [54].

Their presence at the Fe_3C – ferrite interface, representing a prior phase-transformation boundary, together with their parallel alignment to the Fe_3C and GB planes and their comparatively larger size relative to the Cu-PPts within the matrix, all support this conclusion. These observations are consistent with previous reports on the formation of interphase Cu-PPt_{FCC} during austenite decomposition in medium-carbon hypereutectoid steels [54,79]. While the formation of IG Fe_3C and Cu-$PPt_{FCC\text{-}GB}$ is believed to occur during cooling upon phase transformation, the presence of distinct Cu- and C- DZs around the GB containing IG Fe_3C and Cu-$PPt_{FCC\text{-}GB}$ indicates continued growth following the completion of the austenite – ferrite transformation. This interpretation is supported by the persistence of the DZ, which remains stationary rather than being displaced by the migrating phase boundary [54,55,79,84].

In addition to the distinct morphological features identified through APT, STEM, and HRTEM, which suggest a phase-transformation-induced precipitation, the detected OR provides further insight into the formation mechanism, consistent with the probability of transformation-induced precipitation. The Cu-$PPt_{FCC\text{-}GB}$ exhibits an N – W OR with the neighbouring ferrite matrix. While fine and freshly nucleated transformation-induced precipitates typically favour coherent Baker – Nutting (B – N) or Pitsch – Petch (P – P) ORs to minimise lattice misfit and interfacial energy [85,86], other studies have demonstrated that, as these precipitates grow and coarsen – either during cooling or prolonged aging – coherency with the matrix is progressively lost. The consequent increase in interfacial and strain energy drives the system to adopt semi-coherent or incoherent interfaces, manifested as a transition from B – N and P – P to N – W or Kurdjumov – Sachs (K – S) ORs [85,87], both of which provide lower overall energies for larger particles and allow misfit dislocations to accommodate the increasing lattice misfit mismatch [88].

The chemical complexity of GBs and interfaces strongly influences not only the phase transformation and the nature of the transforming interfaces, but also the ORs, often inducing local shifts in ORs [89,90]. As the GBs in this work show chemical heterogeneity at the GBs manifested in the presence of Fe_3C, and Mn, and Ni segregation, a shift from the usual B-N could be related to the GB heterogeneity. The shift in interphase – precipitate ORs due to interfacial heterogeneity is consistent with prior studies that link interphase precipitation kinetics and ORs to the chemical complexity of GBs [89–92]. Accordingly, the N – W OR between the FCC Cu-PPts at the GBs and the surrounding ferritic matrix can arise either from a B – N to N – W transformation accompanying precipitate coarsening, or directly from the complex interfacial chemistry of the GBs.

Although determining the precise onset of copper precipitation in the presence of Fe_3C formation remains challenging due to the competitive nature of GB precipitation, electrical resistivity measurements of copper-alloyed medium-carbon steel have confirmed that Fe_3C precipitation is completed prior to copper precipitation [84]. Additional evidence supporting this sequential precipitation mechanism – first IG Fe_3C, followed by Cu-$PPt_{FCC\text{-}GB}$ – arises from the markedly lower diffusivity of substitutional elements such as copper, compared with interstitial carbon atoms [79]. While the carbon diffusion rates in austenite and ferrite are 10^{-11} to 10^{-12} m/s and 10^{-11} to 10^{-10} m/s respectively, the copper diffusion rates in austenite and ferrite are 10^{-15} to 10^{-16} m/s and 10^{-14} to 10^{-15} m/s respectively [93–95].

Consequently, during the austenite – ferrite transformation and subsequent cooling or aging, carbon diffuses rapidly from the transforming regions, promoting the early formation of IG carbon enrichment and Fe_3C along ferrite – ferrite GBs. In contrast, substitutional elements such as copper require substantially more time to diffuse out of the ferrite matrix as they diffuse significantly more slowly. These pre-existing C-enriched regions and IG Fe_3C layers thus act as preferential nucleation sites for copper atoms that later diffuse from the matrix and precipitate at these interfaces. Therefore, IG carbon enrichment and Fe_3C formation occur first, establishing the microstructural framework that facilitates subsequent Cu-$PPt_{FCC\text{-}GB}$ nucleation and growth at the GBs.

The formation mechanism of IG Cu-PPts may follow pathways analogous to those observed in the ferritic matrix, where Cu-PPts transform sequentially from a BCC structure to intermediate 9R and 3R structures before reaching the FCC equilibrium phase [38,42]. Alternatively, as demonstrated in the austenitic phase, copper can precipitate directly in the FCC structure without intermediate transformations [37]. Given that C-enriched GBs and IG Fe_3C provide preferential nucleation sites for Cu-PPts [54,79,84] owing to their high interfacial energy, estimated to be 0.25–0.7 J/m^2 [96–98], and that GBs act as accelerated diffusion paths for copper precipitation, particularly considering the extremely low solubility of copper in Fe_3C [50], it is plausible that the IG Cu-PPts follow a mechanism akin to that in austenite. In this case, Cu-PPts form directly in the FCC lattice and subsequently coarsen with increasing aging time, without undergoing the displacive transformation sequence observed for copper precipitation within the ferritic matrix. This interpretation is further supported by a comparison between the matrix and IG precipitates: while the Cu-PPts in the matrix exhibit a BCC structure at 120 s and a mixture of BCC and 9R structures at 2400 s, the IG Cu-PPt_{GB} consistently display an FCC lattice irrespective of aging duration, indicating that prolonged aging primarily promotes their growth rather than any further structural transformation.

The scenario of direct nucleation of Cu-$PPt_{FCC\text{-}GB}$ and Fe_3C precipitation was studied in the presented kinetic simulation. Due to the limitations of the mean field approach, the precipitate nucleation on the migrating austenite – ferrite could not be represented. Furthermore, the model architecture required an introduction of the temperature point at which an instantaneous transformation from austenite to ferrite (preserving the chemical composition) occurred, which was set here to 790 °C, as a reasonable mean transformation temperature of the

representative volume element in the MatCalc simulation. This approach allowed us to predict an instantaneous Fe_3C formation reaching a phase fraction value of about 0.4%, which is in excellent agreement with the EBSD measurement. An increase in this phase fraction value was observed during the simulation, as the evaluated equilibrium molar fraction at 550 °C is 3.8%. Nucleation onset for all Cu-PPts forming without any precursor phase (i.e., intragranular BCC clusters, GB precipitates, and precipitates at Fe_3C) is predicted at the cooling stage in a rather tight time interval of 4 s, and it does not allow for any conclusions regarding the nucleation order for these phases. On the other hand, a comparison of the number density at the end of the cooling stage with the maximal value observed in the simulation indicates some preferences. At the start of isothermal holding, all precipitates at Fe_3C, 46% precipitates at the GB, and 3% of BCC clusters had nucleated. These values suggest a clear preference towards IG nucleation over the intragranular one. The order can be explained in terms of the lower nucleation barrier for precipitates formed during the heterogeneous nucleation model as discussed by Miesenberger et al. [68]. This approach accounts for the fact that a newly formed precipitate replaces a part of the microstructure defect (e.g., dislocation, GB, precipitate/matrix boundary), thus releasing the energy stored therein. Undoubtedly, an exact parametrization of the remains approximate and would need further calibration, e.g., the extent of diffusion enhancement for solutes towards the precipitates at Fe_3C, as these Fe_3C precipitates are at the GB, where the diffusion proceeds faster. Nevertheless, the simulation suggests the lower nucleation barrier for the intragranular precipitates to be an important factor in the competition between copper precipitation in the ferrite grains and the one next to these. The effect of carbon enrichment at GBs was not addressed in the presented model, but an extension with the available treatments describing solute trapping (e.g. [99]) could be possible.

Based on the MatCalc simulations, together with comprehensive insights obtained from experimental observations and prior literature on the morphology of interphase Fe_3C and Cu-PPts, a mechanistic hypothesis for the formation of IG Fe_3C and Cu-$PPt_{FCC\text{-}GB}$ is proposed, as illustrated in Fig. 12. Upon cooling from the austenitic range (900 °C) to the aging temperature of 550 °C, the austenite-to-ferrite transformation promotes the formation of interphase and IG Fe_3C, driven by the extremely low solubility of carbon in ferrite [79,81]. Subsequently, copper atoms diffuse out of the supersaturated ferritic matrix, predominantly along GBs and into the IG Fe_3C. These C-enriched GBs and pre-existing IG Fe_3C layers thus serve as preferential nucleation sites for copper precipitation, enabling the accelerated formation of IG (Cu-$PPt_{FCC\text{-}GB}$).

The growth of these IG Cu-PPts proceeds significantly faster than that of their intragranular counterparts through two primary mechanisms. The first is enhanced GB diffusion, where both the GB itself and associated dislocations facilitate accelerated copper transport from the surrounding ferritic matrix into the IG precipitates [100–102]. The second involves Ostwald ripening and/or coalescence-driven coarsening, wherein smaller Cu-PPts of higher chemical potential within the adjacent matrix dissolve and reprecipitate into the larger IG precipitates of lower chemical potential, thereby reaching an energetically favourable configuration [38,55,103–105]. This process results in the development of local C- and Cu- DZs and a PFZ extending up to ~ 10 nm adjacent to the GB.

4.3. *Effect of the IG carbon enrichment and copper precipitates on the GB chemistry and strength, and crack initiation behaviour*

The presence of IG Fe_3C, Cu-PPts, together with the Cu- and C-depleted PFZ, is detrimental to the mechanical integrity of the material, particularly its resistance to IG cracking [106–108]. These features alter the GB chemistry and thereby modify the GB strength [109–113]. The presence of a Cu- and C-depleted PFZ near the GB directly reduces both precipitation strengthening and solid-solution strengthening contributions from interstitial and substitutional solutes. To quantitatively assess the strength reduction within the depleted PFZ relative to the Cu-precipitation-hardened matrix, the losses in solid-solution and precipitation strengthening were evaluated using Eqs. (1) and (2). The loss in solid-solution strengthening was calculated using the empirical Pickering–Gladman [114] relation for ferrite, expressed in Eq. (1):

$$\sigma_{ss} = \sum \hat{K}_i \left(\acute{x}_i\right) \tag{1}$$

where $\acute{x}_i$ is the concentration of the solute element in wt.% and K_i is the proportionality constant for this solute element reported by Pickering and Gladman. Based on APT measurements of the ferritic matrix and the depletion zone adjacent to the GB, the combined reduction in carbon and copper concentrations corresponds to an estimated decrease in solid-solution strengthening of approximately 108 MPa (see Table 5).

In addition to the solid-solution strengthening loss caused by the depletion of carbon and copper near the GB, the formation of a PFZ on one side of the boundary also leads to a reduction in precipitation

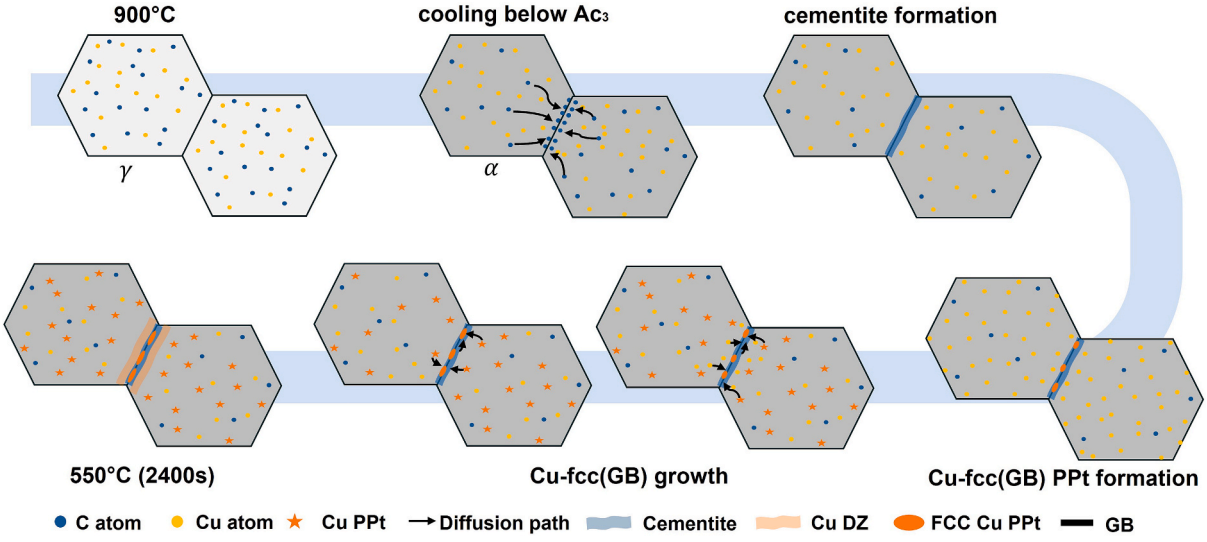

Fig. 12. Schematic illustration representing the sequence of the IG carbon enrichment, followed by copper precipitation nucleation in the matrix and at GBs, and the coarsening behaviour of the Cu-PPts along the C-enriched GBs.

Table 5
Solid solution strengthening (σ_{ss}) contributions of Cu and C in the matrix and depletion zone, and the resulting strengthening drop.

	Solid solution strengthening (σ_{ss}) in MPa				
	K_i	Matrix	DZ	Drop	Total drop in σ_{ss} (Cu + C)
Cu	34.5	18	9	9	108
C	4964	139	40	99	

strengthening, which can be evaluated using Eq. (2):

$$\sigma_{ppt} = 0.538G \times \frac{b\sqrt{f}}{d} \times ln(\frac{d}{2b}) \quad (2)$$

$$f = \frac{4}{3}\ \pi \times r^3 \times N \quad (3)$$

where $G = 81600\ MPa$ is the shear modulus of steel, $b = 0.25nm$ is the Burgers vector, $d = 5\ nm$ is the average precipitate diameter, f is the precipitates volume fraction calculated through Eq. (3), and N is the precipitates number density. With an average precipitates number density determined by APT for the 2400 s condition of N=$1.3 \times 10^{23} m^{-3}$, the calculated volume fraction is about $f = 0.0085$ vol%, and hence, the Cu-PPts population in the matrix provides a precipitation strengthening increment of approximately $\sigma_{ppt} \approx 455$ MPa in the ferritic matrix. This increment is effectively absent inside the PFZ.

The PFZ width observed in the present study (10–15 nm) is sufficiently small that its global effect on the bulk yield strength is expected to be marginal. To quantify this, the threshold approach proposed by Krol [115,116] was adopted for assessing when PFZs begin to reduce yield strength. In this framework [116], the PFZ width w is compared to a critical width w_c, which depends on the mean precipitate radius r, the precipitate volume fraction f, and a geometric factor x , as calculated according to Eq. (4) and Eq. (5):

$$L_{min} = r\sqrt{\frac{\pi x}{f}} \quad (4)$$

$$w_c = 1.7(L_{min} - r) \quad (5)$$

Here L_{min} represents the characteristic spacing between precipitates, r is the mean precipitate radius, f is the precipitate volume fraction, and x is a geometric factor taken as $x = 0.75$ following Krol's original analysis to represent a random, homogeneous precipitate distribution. Using the present alloy parameters ($r = 2.5$ nm, $f = 0.0085$), these relations give $L_{min} \approx 41.6$ nm and a critical PFZ width $w_c \approx 66.5$ nm. Since the measured PFZ width of 10–15 nm is well below this threshold, PFZs in the present alloy are not expected to measurably influence the bulk yield strength, in contrast to other studies reporting PFZs up to ~ 1 μm, where yield strength reductions of 22–25% have been observed [115–118].

Nevertheless, PFZs in the present alloy may still play an important role in local damage initiation, as the local loss of precipitation strengthening within the PFZ creates a sharp strength gradient between the precipitation-hardened matrix and the PFZ and the adjacent C-enriched GB. In particular, the loss of local strength and the resulting stress contrast at the microscale within the softened PFZ adjacent to the grain boundary promote strain localisation and stress concentration in the GB region, which can facilitate micromechanically controlled phenomena such as crack nucleation, initiation, and short-crack propagation either within the PFZ or at its interfaces. In the present alloy, the PFZ is bounded by a C-enriched GB on one side and a precipitation-hardened matrix on the other, further amplifying the local mechanical contrast and increasing the likelihood of damage initiation in the GB region. Because the PFZ is softened by reduced precipitation strengthening and solid-solution strengthening due to C and Cu depletion, and lies between a C-enriched GB and a precipitation-hardened matrix, the strength contrast on both sides of the PFZ makes intergranular crack initiation a plausible scenario via void formation and growth at intergranular Cu-PPts or microcrack formation in IG Fe_3C.

PFZs are widely reported to be mechanically softer than the surrounding matrix and to promote plastic strain localisation, thereby biasing crack initiation and propagation paths toward IG fracture [118,119]. In such softened regions, dislocations preferentially nucleate inside the PFZ rather than at the GB because plastic flow is energetically more favourable in the locally weakened zone. This dislocation activity enhances strain concentration at GBs and increases local stresses at PFZ-matrix and PFZ-boundary interfaces [117,119]. Consequently, PFZs act as channels for strain localisation that promote void or microcrack nucleation and growth, ultimately leading to GB decohesion [120,121].

Direct fractographic and microstructural observations from previous studies support this mechanism, with microcracks frequently observed within PFZs in specimens interrupted prior to failure, demonstrating that fracture can initiate within these softened regions rather than in the precipitation-strengthened matrix [117]. Similar behaviour has also been reported in austenitic steels, where PFZs along GBs weaken the boundary region and lead to IG fracture even when cracks are not strictly coincident with the boundary plane, indicating that the PFZ adjacent to the boundary represents the mechanically weakest region of the microstructure [122]. These observations collectively demonstrate that PFZs promote crack initiation through the combined effects of local softening, intense strain localisation, dislocation pile-up, and strong mechanical contrast with both the GB and the surrounding matrix [117,119,120,122–124].

Additional microstructural features present at the GB further intensify this effect. In particular, the presence of disc-shaped (elliptical) Cu-PPts embedded within IG Fe_3C introduces significant local stress concentrations through two principal mechanisms: (i) lattice strain generated by the misfit between the Cu-PPt_{FCC}, Fe_3C, and the surrounding ferrite matrix[125]; and (ii) geometric notch effects associated with the high aspect ratio of the elliptical precipitates, which produce elevated stresses at their tips [125]. While nanoscale Cu-PPts can enhance local hardening by effectively impeding dislocation motion, suppressing dislocation cell formation, and promoting cyclic hardening [27], this strengthening effect diminishes as precipitates coarsen. Cu-PPts larger than approximately 7.5 nm become less effective barriers to dislocation motion and cell formation, thereby reducing their contribution to cyclic hardening [27].

The IG Fe_3C itself further contributes to the localisation of deformation. Acting as a brittle phase in the GB region, Fe_3C can behave as a geometric notch that intensifies local stress concentrations and promotes heterogeneous plastic flow [126,127]. The resulting dislocation pile-ups, combined with the local strength reduction near the boundary at the PFZ, facilitate crack initiation either within the Fe_3C [128] or at the ferrite–PFZ–Fe_3C interfaces [129]. When these microstructural features are considered together with earlier observations of fatigue behaviour in the same alloy (X21 aged 2400 s), a consistent mechanistic picture emerges. Görzen et al. [35] reported frequent IG crack initiation at ferrite–ferrite GBs, reflecting the reduced defect tolerance of the X21 alloy compared with that of the low-C 2% Cu alloy [33]. These findings, consistent with the present study, demonstrate a strong correlation between interfacial softening effects – arising from the formation of depleted PFZ, IG Fe_3C, and Cu-$PPt_{FCC\text{-}GB}$ and their collective impact on GB strength and resistance to IG crack initiation.

In the X21 alloy, IG crack initiation may therefore proceed via two distinct mechanisms: (i) void nucleation triggered by Cu-$PPt_{FCC\text{-}GB}$ located within or adjacent to a soft depleted PFZ; and (ii) delamination associated with hard IG Fe_3C, as illustrated in Fig. 13. Under applied loading and plastic deformation, the Cu-$PPt_{FCC\text{-}GB}$ act as local stress concentrators, reducing GB cohesion [125,130]. Microvoids may nucleate at precipitate–matrix interfaces through interfacial decohesion, and continued deformation promotes their coalescence, resulting in IG crack initiation through the classical microvoid coalescence mechanism. This mechanism is further intensified by the presence of IG precipitates

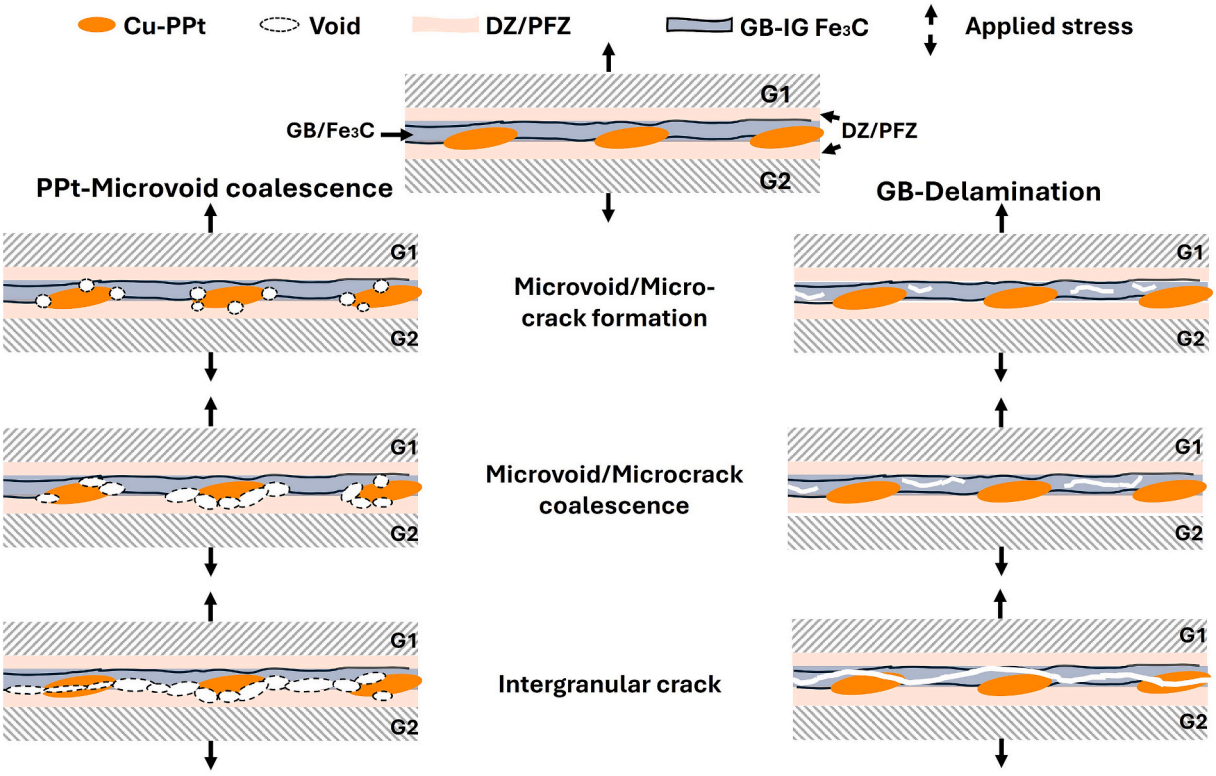

Fig. 13. The possible IG crack initiation mechanism resulting from the IG Fe3C, IG Cu-PPts, and the DZ–PFZ near the GB.

adjacent to mechanically softer regions such as PFZs or DZs near GBs [108,131], as observed in the X21 alloy.

Conversely, IG Fe_3C can promote crack initiation through interfacial delamination or decohesion, in which the boundary separates along the IG Fe_3C–ferrite interface. Microcracks nucleate and progressively coalesce during deformation, ultimately leading to IG fracture. The strong correlation between the presence of IG Fe_3C or carbides in general and GB delamination has been well established in ferritic steels of varying carbon contents [132–135] and is associated with GB embrittlement [135] and increased stress triaxiality within IG Fe_3C layers [136].

Collectively, these results indicate that the presence of Cu-$PPt_{FCC\text{-}GB}$ and IG Fe_3C alongside the presence of soft depleted PFZs is detrimental to GB chemistry and cohesion, thereby facilitating crack initiation and compromising the overall mechanical integrity of the alloy.

5. Summary and conclusions

This study presents a novel experimental observation of copper precipitation behaviour at ferrite–ferrite GBs containing IG Fe_3C in Fe–0.2C–2.0Ni–2.0Cu–0.5Mn (wt.%) steel. Using APT, high-resolution S/TEM, and MatCalc precipitation modeling, the work demonstrates that Cu-PPts at GBs exhibit a distinct precipitation mode compared to those in the ferrite matrix, forming large disc-shaped FCC particles directly, rather than following the conventional B2/BCC → 9R → FCC sequence. The experimental data were used to construct a kinetic model and formulate a mechanistic hypothesis explaining this behaviour.

From the integration of experimental evidence and precipitation-kinetics modeling, the following key conclusions can be drawn:

1. APT and STEM/HRTEM analyses confirm that Cu-PPts in the ferrite matrix follow the conventional martensitic transformation sequence in which coherent B2 clusters and ~ 3 nm Cu-PPt_{BCC} are detected after 120 s of aging, evolving into ~ 5 nm Cu-PPt_{9R} (ABCBCACAB) structures after 2400 s, and finally transforming into equilibrium Cu-PPt_{FCC}.
2. Ferrite–ferrite GBs contain IG Fe_3C associated with carbon enrichment, Ni and Mn segregation, and large disc-shaped Cu-$PPt_{FCC\text{-}GB}$ (~50 × 15 nm) observed after both 120 s and 2400 s of aging. Carbon segregation during the austenite-to-ferrite transformation promotes the formation of IG Fe_3C, which acts as a high-diffusivity path and preferential nucleation site for Cu precipitation at GBs. Consequently, GBs containing IG Fe_3C exhibit nearly five times higher FCC Cu-PPts density and larger precipitate dimensions compared with C-enriched GBs without Fe_3C.
3. Based on the experimental descriptors–size, morphology, lattice structure, and orientation–and literature evidence, it is hypothesized that Cu-$PPt_{FCC\text{-}GB}$ nucleate during austenite decomposition, facilitated by the C-enriched IG Fe_3C. MatCalc simulations parameterized with the experimental input reproduce the observed bimodal size distribution and early Cu-$PPt_{FCC\text{-}GB/Cem}$ formation, supporting the plausibility of this mechanism.
4. IG Fe_3C and Cu precipitation generate Cu- and C-depleted PFZ (approximately 10 nm wide), resulting in estimated reductions of 108 MPa in solid-solution and 455 MPa in precipitation strengthening relative to the matrix. These locally softened regions, together with IG Fe_3C and disc-shaped Cu-$PPt_{FCC\text{-}GB/Cem}$, promote strain localization and may facilitate crack initiation through boundary delamination and/or micro-void coalescence.

Building on this mechanistic framework, future work will employ in-situ synchrotron X-ray diffraction (Sy-XRD) to experimentally verify the proposed hypothesis and to validate the precipitation-kinetics model developed using MatCalc. Real-time observation of the evolution of IG Fe_3C and Cu-$PPt_{FCC\text{-}GB}$ will enable direct correlation between transformation dynamics and predicted thermokinetic pathways. In parallel, the influence of reduced carbon content on the kinetics of IG Fe_3C formation and its interaction with copper precipitation will be systematically investigated. These studies will provide a more quantitative basis for understanding the interplay between GB chemistry, IG Fe_3C, and Cu-$PPt_{FCC\text{-}GB}$ precipitation kinetics, and GB strength, thereby advancing

predictive alloy design for enhanced boundary stability and more effective use of copper as an alloying element.

CRediT authorship contribution statement

Asmaa Elbeltagy: Writing – review & editing, Writing – original draft, Visualization, Validation, Resources, Project administration, Methodology, Investigation, Formal analysis, Data curation, Conceptualization. **Alexander Gramlich:** Writing – review & editing, Supervision, Conceptualization. **Milan Heczko:** Writing – review & editing, Visualization, Validation, Methodology, Investigation, Formal analysis, Data curation, Conceptualization. **Antonín Dlouhý:** Validation, Software, Methodology, Investigation, Formal analysis, Conceptualization. **Tomáš Kruml:** Resources. **Piotr Warczok:** Writing – original draft, Validation, Methodology, Formal analysis, Data curation, Conceptualization. **Ernst Kozeschnik:** Writing – review & editing, Methodology, Conceptualization. **Ulrich Krupp:** Writing – review & editing, Resources, Funding acquisition, Conceptualization.

Declaration of competing interest

The authors declare that they have no known competing financial interests or personal relationships that could have appeared to influence the work reported in this paper.

Acknowledgements

The authors gratefully acknowledge the Deutsche Forschungsgemeinschaft (DFG, German Research Foundation) for funding this work under Grant Number BE 2350/9-2 (project number: 335746905). CzechNanoLab project LM2023051, funded by MEYS CR, is gratefully acknowledged for the financial support of the electron microscopy and characterisation performed at CEITEC Nano Research Infrastructure. The authors would like to thank Dr. Tomáš Babinský, Štěpán Gamanov, and Markéta Gáliková from the Institute of Physics of Materials, Czech Academy of Sciences, for their help with sample preparation and characterization experiments.

Appendix A. Supplementary data

Supplementary data to this article can be found online at https://doi.org/10.1016/j.matdes.2026.116014.

Data availability

Data will be made available on request.

References

[1] Le May and L. M. Schetky, Copper in Iron and Steel. New York, NY, USA: Wiley, 1982.
[2] D. de La Fuente, "Weathering steels," in Encyclopedia of Materials: Metals and Alloys. Amsterdam, The Netherlands: Elsevier, 2022, pp. 129–139.
[3] J. Banas, A. Mazurkiewicz, The effect of copper on passivity and corrosion behaviour of ferritic and ferritic–austenitic stainless steels, Mater. Sci. Eng. A 277 (1–2) (2000) 183–191, https://doi.org/10.1016/S0921-5093(99)00530-4.
[4] H. Huang, A. Juhasz, G. Brunetti, A. Roccisano, and N. Stanford, "Enhanced pitting resistance and antibacterial durability of Cu-bearing stainless steels via tailoring Cu distributions," Materialia, vol. 31, Art. no. 101880, 2023, doi: 10.1016/j.mtla.2023.101880.
[5] G. Grass, C. Rensing, M. Solioz, Metallic copper as an antimicrobial surface, Appl. Environ. Microbiol. 77 (5) (2011) 1541–1547, https://doi.org/10.1128/AEM.02766-10.
[6] A. Gramlich, T. Hinrichs, H. Springer, and U. Krupp, "Recycling-induced copper contamination of a 42CrMo4 quench and tempering steel: Alterations in transformation behaviour and mechanical properties," Steel Res. Int., vol. 94, no. 3, Art. no. 2200623, 2023, doi: 10.1002/srin.202200623.
[7] D. Raabe, et al., Circular steel for fast decarbonization: Thermodynamics, kinetics, and microstructure behind upcycling scrap into high-performance sheet steel, Annu. Rev. Mater. Res. 54 (1) (2024) 247–297, https://doi.org/10.1146/annurev-matsci-080222-123648.
[8] S.S. Xu, et al., Precipitation kinetics and mechanical properties of nanostructured steels with Mo additions, Mater. Res. Lett. 8 (5) (2020) 187–194, https://doi.org/10.1080/21663831.2020.1734976.
[9] Q. Liu, W. Liu, X. Xiong, Correlation of Cu precipitation with austenite–ferrite transformation in a continuously cooled multicomponent steel: an atom probe tomography study, J. Mater. Res. 27 (7) (2012) 1060–1067, https://doi.org/10.1557/jmr.2012.54.
[10] G. I. Sil'man, V. V. Kamynin, and A. A. Tarasov, "Influence of copper on the structure and properties of low-carbon steels," Met. Sci. Heat Treat., vol. 45, no. 7–8, pp. 254–258, 2003, doi: 10.1023/A:1027320116132.
[11] J. Wang, C. Li, X. Di, and D. Wang, "Effect of Cu content on microstructure and mechanical properties for high-strength deposited metals strengthened by nano-precipitation," Metals, vol. 12, no. 8, Art. no. 1360, 2022, doi: 10.3390/met12081360.
[12] Z.B. Jiao, J.H. Luan, W. Guo, J.D. Poplawsky, C.T. Liu, Atom-probe study of Cu and NiAl nanoscale precipitation and interfacial segregation in a nanoparticle-strengthened steel, Mater. Res. Lett. 5 (8) (2017) 562–568, https://doi.org/10.1080/21663831.2017.1364675.
[13] Q. Shen, D. Huang, W. Liu, F. Li, and Q. Lu, "Effect of Cu content on the precipitation behaviour of Cu-rich and NiAl phases in steel," Mater. Charact., vol. 187, Art. no. 111849, 2022, doi: 10.1016/j.matchar.2022.111849.
[14] M. Kapoor, D. Isheim, G. Ghosh, S. Vaynman, M.E. Fine, Y.-W. Chung, Aging characteristics and mechanical properties of 1600 MPa body-centred cubic Cu and B2-NiAl precipitation-strengthened ferritic steel, Acta Mater. 73 (2014) 56–74, https://doi.org/10.1016/j.actamat.2014.03.051.
[15] Z.B. Jiao, J.H. Luan, M.K. Miller, C.T. Liu, Precipitation mechanism and mechanical properties of an ultra-high-strength steel hardened by nanoscale NiAl and Cu particles, Acta Mater. 97 (2015) 58–67, https://doi.org/10.1016/j.actamat.2015.06.063.
[16] K. Jin, et al., Enhanced strength–ductility synergy in an ultra-strong copper alloy via coherent nanoprecipitates and stress-induced twinning, Mater. Res. Lett. 12 (4) (2024) 281–289, https://doi.org/10.1080/21663831.2024.2319927.
[17] M. Sun, Y. Xu, and T. Xu, "Cu precipitation behaviours and microscopic mechanical characteristics of a novel ultra-low carbon steel," Materials, vol. 13, no. 16, Art. no. 3571, 2020, doi: 10.3390/ma13163571.
[18] L. J. Wang et al., "Influences of Cu on microstructure and mechanical properties in Fe–Ni–Al ultra-strong maraging steels," Mater. Sci. Eng. A, vol. 886, Art. no. 145724, 2023, doi: 10.1016/j.msea.2023.145724.
[19] Z. B. Jiao, J. H. Luan, M. K. Miller, C. Y. Yu, and C. T. Liu, "Group precipitation and age hardening of nanostructured Fe-based alloys with ultra-high strength," Sci. Rep., vol. 6, Art. no. 21364, 2016, doi: 10.1038/srep21364.
[20] Z.B. Jiao, J.H. Luan, M.K. Miller, Y.W. Chung, C.T. Liu, Co-precipitation of nanoscale particles in steels with ultra-high strength for a new era, Mater. Today 20 (3) (2017) 142–154, https://doi.org/10.1016/j.mattod.2016.07.002.
[21] Z. Xu et al., "Tailoring the austenite fraction of a Cu- and Ni-containing medium-Mn steel via warm rolling," Metals, vol. 11, no. 12, Art. no. 1888, 2021, doi: 10.3390/met11121888.
[22] Y. Li, et al., The austenite reversion and co-precipitation behaviour of an ultra-low-carbon medium-manganese quenching–partitioning–tempering steel, Acta Mater. 146 (2018) 126–141, https://doi.org/10.1016/j.actamat.2017.12.035.
[23] A. Elbeltagy, Z. Xu, X. Shen, U. Krupp, and W. Song, "Yield strength enhancement without ductility loss through controlling the intercritical annealing time in medium-Mn steels," Adv. Eng. Mater., vol. 25, no. 15, Art. no. 2300067, 2023, doi: 10.1002/adem.202300067.
[24] M.E. Fine, S. Vaynman, D. Isheim, Y.-W. Chung, S.P. Bhat, C.H. Hahin, A new paradigm for designing high-fracture-energy steels, Metall. Mater. Trans. A 41 (13) (2010) 3318–3325, https://doi.org/10.1007/s11661-010-0485-y.
[25] M. Kapoor, D. Isheim, S. Vaynman, M.E. Fine, Y.-W. Chung, Effects of increased alloying element content on NiAl-type precipitate formation, loading-rate sensitivity, and ductility of Cu- and NiAl-precipitation-strengthened ferritic steels, Acta Mater. 104 (2016) 166–171, https://doi.org/10.1016/j.actamat.2015.11.041.
[26] J. Weertman, Mason's dislocation relaxation mechanism, Phys. Rev. 101 (4) (1956) 1429–1430, https://doi.org/10.1103/PhysRev.101.1429.
[27] J.T. McGrath, W.J. Bratina, Fatigue of an Fe-1.5% Cu alloy containing stable, non-coherent precipitate particles, Philos. Mag. 21 (173) (1970) 1087–1091, https://doi.org/10.1080/14786437008238493.
[28] R.A. Fournelle, E.A. Grey, M.E. Fine, Fatigue behaviour of a precipitation-hardening Ni–Al–Cu medium-carbon steel, Metall. Trans. A 7 (5) (1976) 669–682, https://doi.org/10.1007/BF03186798.
[29] T. Yokoi, M. Takahashi, N. Maruyama, M. Sugiyama, Cyclic stress response and fatigue behaviour of Cu-added ferritic steels, J. Mater. Sci. 36 (24) (2001) 5757–5765, https://doi.org/10.1023/A:1012939601936.
[30] H. Nakano, T. Miyazawa, H. Shuto, T. Fujii, Development of cell structure and crack initiation during fatigue of an Fe-3 mass%Si alloy, Tetsu-to-Hagane 109 (1) (2023) 76–85, https://doi.org/10.2355/tetsutohagane.TETSU-2022-078.
[31] S. Hamada, et al., Ductile-to-brittle transition in tensile failure due to shear-affected zone with a stress-concentration source: a comparative study on punched-plate tensile-failure characteristics of precipitation-hardened and dual-phase steels, Int. J. Fract. 212 (2) (2018) 237–248, https://doi.org/10.1007/s10704-018-0304-9.
[32] V. K. Verma, C. K. Gopalakrishnan, S. Hamada, T. Yokoi, and H. Noguchi, "Effect of strain localization on fatigue properties of precipitation-hardened steel with an arbitrarily length crack," Int. J. Fatigue, vol. 143, Art. no. 106017, 2021, doi: 10.1016/j.ijfatigue.2020.106017.

[33] D. Görzen et al., "Influence of Cu precipitates and C content on the defect tolerance of steels," Int. J. Fatigue, vol. 144, Art. no. 106042, 2021, doi: 10.1016/j.ijfatigue.2020.106042.

[34] D. Görzen, H. Schwich, B. Blinn, W. Bleck, and T. Beck, "Influence of different precipitation conditions of Cu on the quasi-static and cyclic deformation behaviour of Cu alloyed steels with different carbon contents," Int. J. Fatigue, vol. 136, Art. no. 105587, 2020, doi: 10.1016/j.ijfatigue.2020.105587.

[35] D. Görzen, B. Blinn, and T. Beck, "Influence of the C content on the fatigue crack initiation and short crack behaviour of Cu alloyed steels," Metals, vol. 13, no. 6, Art. no. 1024, 2023, doi: 10.3390/met13061024.

[36] A.K. Niessen, F.R. de Boer, R. Boom, P.F. de Châtel, W. Mattens, A.R. Miedema, Model predictions for the enthalpy of formation of transition metal alloys II, Calphad 7 (1) (1983) 51–70, https://doi.org/10.1016/0364-5916(83)90030-5.

[37] T. Xi, et al., Copper precipitation behaviour and mechanical properties of Cu-bearing 316L austenitic stainless steel: a comprehensive cross-correlation study, Mater. Sci. Eng. A 675 (2016) 243–252, https://doi.org/10.1016/j.msea.2016.08.058.

[38] W. Ostwald, Studien über die Bildung und Umwandlung fester Körper, Z. Phys. Chem. 22U (1) (1897) 289–330, https://doi.org/10.1515/zpch-1897-2233.

[39] A. Umantsev, G.B. Olson, Ostwald ripening in multicomponent alloys, Scr. Metall. Mater. 29 (8) (1993) 1135–1140, https://doi.org/10.1016/0956-716X(93)90191-T.

[40] Y.-U. Heo, Y.-K. Kim, J.-S. Kim, J.-K. Kim, Phase transformation of Cu precipitates from BCC to FCC in Fe–3Si–2Cu alloy, Acta Mater. 61 (2) (2013) 519–528, https://doi.org/10.1016/j.actamat.2012.09.068.

[41] P.J. Othen, M.L. Jenkins, G.D.W. Smith, High-resolution electron microscopy studies of the structure of Cu precipitates in α-Fe, Philos. Mag. A 70 (1) (1994) 1–24, https://doi.org/10.1080/01418619408242533.

[42] G. Han, Z.J. Xie, Z.Y. Li, B. Lei, C.J. Shang, R. Misra, Evolution of crystal structure of Cu precipitates in a low-carbon steel, Mater. Des. 135 (2017) 92–101, https://doi.org/10.1016/j.matdes.2017.08.054.

[43] M. Andrade, M. Chandrasekaran, L. Delaey, The basal plane stacking faults in 18R martensite of copper-base alloys, Acta Metall. 32 (10) (1984) 1809–1816, https://doi.org/10.1016/0001-6160(84)90237-2.

[44] Y.R. Wen, et al., Synergistic alloying effect on microstructural evolution and mechanical properties of Cu precipitation-strengthened ferritic alloys, Acta Mater. 61 (20) (2013) 7726–7740, https://doi.org/10.1016/j.actamat.2013.09.011.

[45] Z.B. Jiao, J.H. Luan, Z.W. Zhang, M.K. Miller, W.B. Ma, C.T. Liu, Synergistic effects of Cu and Ni on nanoscale precipitation and mechanical properties of high-strength steels, Acta Mater. 61 (16) (2013) 5996–6005, https://doi.org/10.1016/j.actamat.2013.06.040.

[46] F. Soisson, A. Barbu, G. Martin, Monte Carlo simulations of copper precipitation in dilute iron-copper alloys during thermal aging and under electron irradiation, Acta Mater. 44 (9) (1996) 3789–3800, https://doi.org/10.1016/1359-6454(95)00447-5.

[47] S. Cui, M. Mamivand, and D. Morgan, "Simulation of Cu precipitation in Fe–Cu dilute alloys with cluster mobility," Mater. Des., vol. 191, Art. no. 108574, 2020, doi: 10.1016/j.matdes.2020.108574.

[48] E. Ilia, P. Plamondon, J.-P. Masse, and G. L'Espérance, "Copper precipitation at engine operating temperatures in powder-forged connecting rods manufactured with Fe–Cu–C alloys," Mater. Sci. Eng. A, vol. 767, Art. no. 138383, 2019, doi: 10.1016/j.msea.2019.138383.

[49] W.H. Zhou, H. Guo, Z.J. Xie, C.J. Shang, R. Misra, Copper precipitation and its impact on mechanical properties in a low-carbon microalloyed steel processed by a three-step heat treatment, Mater. Des. 63 (2014) 42–49, https://doi.org/10.1016/j.matdes.2014.05.059.

[50] K. Osamura, et al., SANS study of phase decomposition in Fe–Cu alloy with Ni and Mn addition, ISIJ Int. 34 (4) (1994) 346–354, https://doi.org/10.2355/isijinternational.34.346.

[51] S.K. Ghosh, A. Haldar, P.P. Chattopadhyay, On the Cu precipitation behaviour in thermomechanically processed low-carbon microalloyed steels, Mater. Sci. Eng. A 519 (1–2) (2009) 88–93, https://doi.org/10.1016/j.msea.2009.05.013.

[52] J. Dölling, S. F. Kracun, U. Prahl, M. Fehlbier, and A. Zilly, "A comparative differential scanning calorimetry study of precipitation-hardenable copper-based alloys with optimized strength and high conductivity," Metals, vol. 13, no. 1, Art. no. 150, 2023, doi: 10.3390/met13010150.

[53] A.N. Bhagat, S.K. Pabi, S. Ranganathan, O.N. Mohanty, Study on copper precipitation during continuous heating and cooling of HSLA steels using electrical resistivity, Mater. Sci. Technol. 23 (2) (2007) 158–164, https://doi.org/10.1179/174328407X157218.

[54] T. Chairuangsri, The precipitation of copper in abnormal ferrite and pearlite in hyper-eutectoid steels, Acta Mater. 48 (15) (2000) 3931–3949, https://doi.org/10.1016/S1359-6454(00)00176-2.

[55] V.A. Hosseini, et al., Precipitation kinetics of Cu-rich particles in super duplex stainless steels, J. Mater. Res. Technol. 15 (2021) 3951–3964, https://doi.org/10.1016/j.jmrt.2021.10.032.

[56] P.J. Phillips, M.C. Brandes, M.J. Mills, M. de Graef, Diffraction contrast STEM of dislocations: imaging and simulations, Ultramicroscopy 111 (9–10) (2011) 1483–1487, https://doi.org/10.1016/j.ultramic.2011.07.001.

[57] M. Heczko, et al., Atomic-resolution characterisation of strengthening nanoparticles in a new high-temperature-capable 43Fe–25Ni–22.5Cr austenitic stainless steel, Mater. Sci. Eng. A 719 (2018) 49–60, https://doi.org/10.1016/j.msea.2018.02.004.

[58] E. Kozeschnik, "Mean-field microstructure kinetics modeling," in Encyclopedia of Materials: Metals and Alloys. Amsterdam, The Netherlands: Elsevier, 2022, pp. 521–526.

[59] E. Kozeschnik, J. Svoboda, R. Radis, and F. D. Fischer, "Mean-field model for the growth and coarsening of stoichiometric precipitates at grain boundaries," Model. Simul. Mater. Sci. Eng., vol. 18, no. 1, Art. no. 015011, 2010, doi: 10.1088/0965-0393/18/1/015011.

[60] P. Haasen and G. Thomas, Eds., Decomposition of Alloys: The Early Stages. Amsterdam, The Netherlands: Elsevier, 1984.

[61] J. Svoboda, F.D. Fischer, P. Fratzl, E. Kozeschnik, Modelling of kinetics in multi-component multi-phase systems with spherical precipitates, Mater. Sci. Eng. A 385 (1–2) (2004) 166–174, https://doi.org/10.1016/j.msea.2004.06.018.

[62] E. Kozeschnik, J. Svoboda, P. Fratzl, F.D. Fischer, Modelling of kinetics in multi-component multi-phase systems with spherical precipitates, Mater. Sci. Eng. A 385 (1–2) (2004) 157–165, https://doi.org/10.1016/j.msea.2004.06.016.

[63] E. Kozeschnik, J. Svoboda, F.D. Fischer, Shape factors in modeling of precipitation, Mater. Sci. Eng. A 441 (1–2) (2006) 68–72, https://doi.org/10.1016/j.msea.2006.08.088.

[64] K.C. Russell, Nucleation in solids: the induction and steady condition effects, Adv. Colloid Interface Sci. 13 (3–4) (1980) 205–318, https://doi.org/10.1016/0001-8686(80)80003-0.

[65] B. Sonderegger, E. Kozeschnik, Generalized nearest-neighbor broken-bond analysis of randomly oriented coherent interfaces in multicomponent Fcc and Bcc structures, Metall. Mater. Trans. A 40 (3) (2009) 499–510, https://doi.org/10.1007/s11661-008-9752-6.

[66] B. Sonderegger, E. Kozeschnik, Size dependence of the interfacial energy in the generalized nearest-neighbor broken-bond approach, Scr. Mater. 60 (8) (2009) 635–638, https://doi.org/10.1016/j.scriptamat.2008.12.025.

[67] B. Sonderegger, E. Kozeschnik, Interfacial energy of diffuse phase boundaries in the generalized broken-bond approach, Metall. Mater. Trans. A 41 (12) (2010) 3262–3269, https://doi.org/10.1007/s11661-010-0370-8.

[68] B. Miesenberger, E. Kozeschnik, B. Milkereit, P. Warczok, and E. Povoden-Karadeniz, "Computational analysis of heterogeneous nucleation and precipitation in AA6005 Al-alloy during continuous cooling DSC experiments," Materialia, vol. 25, Art. no. 101538, 2022, doi: 10.1016/j.mtla.2022.101538.

[69] G. Stechauner, E. Kozeschnik, Thermo-kinetic modeling of Cu precipitation in α-Fe, Acta Mater. 100 (2015) 135–146, https://doi.org/10.1016/j.actamat.2015.08.042.

[70] P. Warczok, J. Ženíšek, E. Kozeschnik, Atomistic and continuums modeling of cluster migration and coagulation in precipitation reactions, Comput. Mater. Sci 60 (2012) 59–65, https://doi.org/10.1016/j.commatsci.2012.02.033.

[71] B. Gault, M. P. Moody, J. M. Cairney, and S. P. Ringer, Atom Probe Microscopy. New York, NY, USA: Springer, 2012.

[72] T. F. Kelly and M. K. Miller, "Invited review article: Atom probe tomography," Rev. Sci. Instrum., vol. 78, no. 3, Art. no. 031101, 2007, doi: 10.1063/1.2709758.

[73] M. Thuvander, D. Shinde, A. Rehan, S. Ejnermark, K. Stiller, Improving compositional accuracy in APT analysis of carbides using a decreased detection efficiency, Microsc. Microanal. 25 (2) (2019) 454–461, https://doi.org/10.1017/S1431927619000424.

[74] L. Morsdorf, A. Kashiwar, C. Kübel, and C. C. Tasan, "Carbon segregation and cementite precipitation at grain boundaries in quenched and tempered lath martensite," Mater. Sci. Eng. A, vol. 862, Art. no. 144369, 2023, doi: 10.1016/j.msea.2022.144369.

[75] S.R. Goodman, S.S. Brenner, J.R. Low, An FIM-atom probe study of the precipitation of copper from lron-1.4 at. pct copper. Part II: atom probe analyses, Metall. Trans. 4 (10) (1973) 2371–2378, https://doi.org/10.1007/BF02669377.

[76] S.Y. Hu, Y.L. Li, K. Watanabe, Calculation of internal stresses around Cu precipitates in the bcc Fe matrix by atomic simulation, Model. Simul. Mater. Sci. Eng. 7 (4) (1999) 641–655, https://doi.org/10.1088/0965-0393/7/4/312.

[77] C. Ophus et al., "Efficient linear phase contrast in scanning transmission electron microscopy with matched illumination and detector interferometry," Nat. Commun., vol. 7, Art. no. 10719, 2016, doi: 10.1038/ncomms10719.

[78] W. Wang, W. Cai, Dynamic observation and motion tracking of individual gold atoms with HAADF-STEM imaging, RSC Adv. 11 (19) (2021) 11057–11061, https://doi.org/10.1039/D0RA09799C.

[79] G. Fourlaris, A.J. Baker, G.D. Papadimitriou, Microscopic characterisation of ε-Cu interphase precipitation in hypereutectoid Fe-C-Cu alloys, Acta Metall. Mater. 43 (7) (1995) 2589–2604, https://doi.org/10.1016/0956-7151(94)00474-V.

[80] F.A. Khalid, Copper precipitation in M23C6 grain boundary carbides in alloy steel, Scr. Mater. 44 (5) (2001) 797–801, https://doi.org/10.1016/s1359-6462(00)00659-x.

[81] J.A. Lobo, G.H. Geiger, Thermodynamics and solubility of carbon in ferrite and ferritic Fe-Mo alloys, Metall. Trans. A 7 (8) (1976) 1347–1357, https://doi.org/10.1007/BF02658820.

[82] R.W.K. Honeycombe, R.F. Mehl, Transformation from austenite in alloy steels, Metall. Trans. A 7 (7) (1976) 915–936, https://doi.org/10.1007/BF02644057.

[83] X. Zhang, T. Hickel, J. Rogal, S. Fähler, R. Drautz, J. Neugebauer, Structural transformations among austenite, ferrite and cementite in Fe–C alloys: a unified theory based on ab initio simulations, Acta Mater. 99 (2015) 281–289, https://doi.org/10.1016/j.actamat.2015.07.075.

[84] J.-G. Jung, M. Jung, S.-M. Lee, E. Shin, H.-C. Shin, Y.-K. Lee, Cu precipitation kinetics during martensite tempering in a medium C steel, J. Alloys Compd. 553 (2013) 299–307, https://doi.org/10.1016/j.jallcom.2012.11.108.

[85] X. Li et al., "A Systematical Evaluation of the Crystallographic Orientation Relationship between MC Precipitates and Ferrite Matrix in HSLA Steels," Materials, vol. 15, no. 11, Art. no. 3967, 2022, doi: 10.3390/ma15113967.

[86] J. Cong et al., "The Impact of Interphase Precipitation on the Mechanical Behavior of Fire-Resistant Steels at an Elevated Temperature," Materials, vol. 13, no. 19, Art. no. 4294, 2020, doi: 10.3390/ma13194294.
[87] H.W. Yen, C.Y. Chen, T.Y. Wang, C.Y. Huang, J.R. Yang, Orientation relationship transition of nanometre sized interphase precipitated TiC carbides in Ti bearing steel, Mater. Sci. Technol. 26 (4) (2010) 421–430, https://doi.org/10.1179/026708309X12512744154207.
[88] A. Ardell, On the coarsening of grain boundary precipitates, Acta Metall. 20 (4) (1972) 601–609, https://doi.org/10.1016/0001-6160(72)90015-6.
[89] I. Bikmukhametov et al., "Interface characteristics and precipitation during the austenite-to-ferrite transformation of a Ti-Mo microalloyed steel," J. Alloys Compd., vol. 893, Art. no. 162224, 2022, doi: 10.1016/j.jallcom.2021.162224.
[90] Y.-J. Zhang, G. Miyamoto, K. Shinbo, T. Furuhara, Quantitative measurements of phase equilibria at migrating α/γ interface and dispersion of VC interphase precipitates: Evaluation of driving force for interphase precipitation, Acta Mater. 128 (2017) 166–175, https://doi.org/10.1016/j.actamat.2017.02.020.
[91] E. Pereloma, J. Wang, H. Beladi, N. Singh, and I. Timokhina, "Solute segregation, clustering and interphase precipitation in Ti-Mo-Nb microalloyed steel studied by correlated electron backscattering diffraction and atom probe tomography," Mater. Charact., vol. 216, Art. no. 114273, 2024, doi: 10.1016/j.matchar.2024.114273.
[92] S. Clark, V. Janik, Y. Lan, S. Sridhar, Interphase precipitation – an interfacial segregation model, ISIJ Int. 57 (3) (2017) 524–532, https://doi.org/10.2355/isijinternational.ISIJINT-2016-544.
[93] P. Shewmon, Diffusion in Solids. Cham, Switzerland: Springer International Publishing, 2016.
[94] R. W. Cahn and P. Haasen, Physical metallurgy, 4th ed. Amsterdam, The Netherlands: North-Holland, 1996.
[95] T. Gladman, Physical metallurgy. Leeds, UK: Maney, 2002.
[96] P. Deb, M.C. Chaturvedi, Coarsening behavior of cementite particles in a ferrite matrix in 10B30 steel, Metallography 15 (4) (1982) 341–354, https://doi.org/10.1016/0026-0800(82)90026-X.
[97] J. Kramer, G. Pound, R. Mehl, The free energy of formation and the interfacial enthalpy in pearlite, Acta Metall. 6 (12) (1958) 763–771, https://doi.org/10.1016/0001-6160(58)90051-8.
[98] H. Mao, C. Zeng, Z. Zhang, X. Shuai, and S. Tang, "The Effect of Lattice Misfits on the Precipitation at Dislocations: Phase-Field Crystal Simulation," Materials, vol. 16, no. 18, Art. no. 6307, 2023, doi: 10.3390/ma16186307.
[99] J. Svoboda, F.D. Fischer, Modelling for hydrogen diffusion in metals with traps revisited, Acta Mater. 60 (3) (2012) 1211–1220, https://doi.org/10.1016/j.actamat.2011.11.025.
[100] Q. Liu, S. Zhao, Cu precipitation on dislocation and interface in quench-aged steel, MRS Commun. 2 (4) (2012) 127–132, https://doi.org/10.1557/mrc.2012.21.
[101] R. M. German, Sintering: from Empirical Observations to Scientific Principles. Amsterdam, The Netherlands: Elsevier, 2014.
[102] J. Jaseliunaite and A. Galdikas, "Kinetic Modeling of Grain Boundary Diffusion: The Influence of Grain Size and Surface Processes," Materials, vol. 13, no. 5, Art. no. 1051, 2020, doi: 10.3390/ma13051051.
[103] R. M. German, "Thermodynamic and Kinetic Treatments," in Sintering: from Empirical Observations to Scientific Principles. Amsterdam, The Netherlands: Elsevier, 2014, pp. 183–226.
[104] J. Wang, Z. Wang, X. Wang, Q. Yang, X. Jin, L. Wang, Strengthening effect of nanoscale precipitation and transformation induced plasticity in a hot rolled copper-containing ferrite-based lightweight steel, Scr. Mater. 129 (2017) 25–29, https://doi.org/10.1016/j.scriptamat.2016.10.025.
[105] S. Chen, Y. Li, S. Shi, S. Jin, Quantitative phase-field simulation of composition partition and separation kinetics of nanoscale phase in Fe-Cr-Al alloy, J. Nanomater. 2019 (2019) 1–11, https://doi.org/10.1155/2019/6862390.
[106] D. Scheiber, T. Jechtl, J. Svoboda, F.D. Fischer, L. Romaner, On solute depletion zones along grain boundaries during segregation, Acta Mater. 182 (2020) 100–107, https://doi.org/10.1016/j.actamat.2019.10.040.
[107] K. Leitner, et al., How grain boundary chemistry controls the fracture mode of molybdenum, Mater. Des. 142 (2018) 36–43, https://doi.org/10.1016/j.matdes.2018.01.012.
[108] S. Lynch, A review of underlying reasons for intergranular cracking for a variety of failure modes and materials and examples of case histories, Eng. Fail. Anal. 100 (2019) 329–350, https://doi.org/10.1016/j.engfailanal.2019.02.027.
[109] G. Sha, L. Yao, X. Liao, S.P. Ringer, Z. Chao Duan, T.G. Langdon, Segregation of solute elements at grain boundaries in an ultrafine grained Al-Zn-Mg-Cu alloy, Ultramicroscopy 111 (6) (2011) 500–505, https://doi.org/10.1016/j.ultramic.2010.11.013.
[110] H. Zhao, et al., Segregation assisted grain boundary precipitation in a model Al-Zn-Mg-Cu alloy, Acta Mater. 156 (2018) 318–329, https://doi.org/10.1016/j.actamat.2018.07.003.
[111] J. Kameda, C.J. McMahon, The effects of Sb, Sn, and P on the strength of grain boundaries in a Ni-Cr Steel, Metall. Trans. A 12 (1) (1981) 31–37, https://doi.org/10.1007/BF02648505.
[112] S.S. Hwang, Y.S. Lim, S.W. Kim, D.J. Kim, H.P. Kim, Role of grain boundary carbides in cracking behavior of Ni base alloys, Nucl. Eng. Technol. 45 (1) (2013) 73–80, https://doi.org/10.5516/NET.07.2012.013.
[113] P. Lejček, M. Šob, V. Paidar, Interfacial segregation and grain boundary embrittlement: an overview and critical assessment of experimental data and calculated results, Prog. Mater Sci. 87 (2017) 83–139, https://doi.org/10.1016/j.pmatsci.2016.11.001.
[114] T.N. Baker, Microalloyed steels, Ironmaking Steelmaking 43 (4) (2016) 264–307, https://doi.org/10.1179/1743281215Y.0000000063.
[115] T. Krol, D. Baither, E. Nembach, Quantification of the detrimental effects of precipitate free zones on the yield strength of a superalloy, Scr. Mater. 48 (8) (2003) 1189–1194, https://doi.org/10.1016/S1359-6462(02)00566-3.
[116] T. Krol, D. Baither, E. Nembach, The formation of precipitate free zones along grain boundaries in a superalloy and the ensuing effects on its plastic deformation, Acta Mater. 52 (7) (2004) 2095–2108, https://doi.org/10.1016/j.actamat.2004.01.011.
[117] A. Peterson and I. Baker, "The formation mechanism, growth, and effect on the mechanical properties of precipitate free zones in the alumina-forming austenitic stainless steel Fe–20Cr–30Ni–2Nb–5Al during creep," Mater. Sci. Eng. A, vol. 820, Art. no. 141561, 2021, doi: 10.1016/j.msea.2021.141561.
[118] J.J. Hoyt, A mean field description of the kinetics of precipitate free zone formation, Scr. Mater. 37 (12) (1997) 2033–2039, https://doi.org/10.1016/S1359-6462(97)00369-2.
[119] M. Khadyko, C.D. Marioara, I.G. Ringdalen, S. Dumoulin, O.S. Hopperstad, Deformation and strain localization in polycrystals with plastically heterogeneous grains, Int. J. Plast 86 (2016) 128–150, https://doi.org/10.1016/j.ijplas.2016.08.005.
[120] F. Li, Z. Guo, G. Chen, S. Chen, K. Chen, and C. Zhu, "Probing the micro-mechanism of precipitate-strengthened alloys with precipitate free zone: An experimental and theoretical study," Int. J. Plast., vol. 181, Art. no. 104085, 2024, doi: 10.1016/j.ijplas.2024.104085.
[121] M. M. Arani, N. S. Ramesh, X. Wang, N. Parson, M. Li, and W. J. Poole, "The localization of plastic deformation in the precipitate free zone of an Al-Mg-Si-Mn alloy," Acta Mater., vol. 231, Art. no. 117872, 2022, doi: 10.1016/j.actamat.2022.117872.
[122] A. Hamada, F. Aarab, R. Schwaiger, and T. Allam, "Exploring high-temperature deformation and damage behaviour in high-performance ferritic (HiperFerSCR) steel with Laves phase particles," Mater. Sci. Eng. A, vol. 908, Art. no. 146771, 2024, doi: 10.1016/j.msea.2024.146771.
[123] A. Peterson and I. Baker, "Microstructural evolution of Fe–20Cr–30Ni–2Nb–5Al AFA steel during creep at 760 °C," Mater. Sci. Eng. A, vol. 806, Art. no. 140602, 2021, doi: 10.1016/j.msea.2020.140602.
[124] W. Liu, Q. Qiu, Y. Chen, C. Tang, Simulation of PFZ on intergranular fracture based on XFEM and CPFEM, J. Cent. South Univ. 23 (10) (2016) 2500–2505, https://doi.org/10.1007/s11771-016-3309-4.
[125] S. Biswal, R. K. Barik, S. Neogy, R. Tewari, A. Dutta, and D. Chakrabarti, "Unravelling the mechanisms of copper precipitation-induced strengthening in austenitic stainless steels: An atomistic approach," Materialia, vol. 32, Art. no. 101962, 2023, doi: 10.1016/j.mtla.2023.101962.
[126] J.R. Rice, J.-S. Wang, Embrittlement of interfaces by solute segregation, Mater. Sci. Eng. A 107 (1989) 23–40, https://doi.org/10.1016/0921-5093(89)90372-9.
[127] E. Vasilev and M. Knezevic, "Role of microstructural heterogeneities in damage formation and fracture of oligocrystalline Mg under tensile loading," Mater. Sci. Eng. A, vol. 827, Art. no. 142096, 2021, doi: 10.1016/j.msea.2021.142096.
[128] T. Lindley, G. Oates, C. Richards, A critical of carbide cracking mechanisms in ferride/carbide aggregates, Acta Metall. 18 (11) (1970) 1127–1136, https://doi.org/10.1016/0001-6160(70)90103-3.
[129] M. Koyama, et al., Elucidation of the effects of cementite morphology on damage formation during monotonic and cyclic tension in binary low carbon steels using in situ characterization, Mater. Sci. Eng. A 667 (2016) 358–367, https://doi.org/10.1016/j.msea.2016.05.029.
[130] J. Schijve, Ed., Fatigue of Structures and Materials. Dordrecht, The Netherlands: Springer Netherlands, 2009.
[131] P. Unwin, G. Lorimer, R. Nicholson, The origin of the grain boundary precipitate free zone, Acta Metall. 17 (11) (1969) 1363–1377, https://doi.org/10.1016/0001-6160(69)90154-0.
[132] W. Yan, W. Sha, L. Zhu, W. Wang, Y.-Y. Shan, K. Yang, Delamination Fracture Related to Tempering in a High-Strength Low-Alloy Steel, Metall. Mater. Trans. A 41 (1) (2010) 159–171, https://doi.org/10.1007/s11661-009-0068-y.
[133] J.-C. Han, J.-B. Seol, M. Jafari, J.-E. Kim, S.-J. Seo, C.-G. Park, Competitive grain boundary segregation of phosphorus and carbon governs delamination crack in a ferritic steel, Mater Charact 145 (2018) 454–460, https://doi.org/10.1016/j.matchar.2018.08.060.
[134] A.J. DeArdo, An investigation of the mechanism of splitting which occurs in tensile specimens of high strength low alloy steels, Metall. Trans. A 8 (3) (1977) 473–486, https://doi.org/10.1007/BF02661759.
[135] B.L. Bramfitt, A.R. Marder, A study of the delamination behavior of a very low-carbon steel, Metall. Trans. A 8 (8) (1977) 1263–1273, https://doi.org/10.1007/BF02643841.
[136] R. Song, D. Ponge, D. Raabe, Mechanical properties of an ultrafine grained C–Mn steel processed by warm deformation and annealing, Acta Mater. 53 (18) (2005) 4881–4892, https://doi.org/10.1016/j.actamat.2005.07.009.